Bioactive Materials 50 (2025) 95–115

Contents lists available at ScienceDirect

Bioactive Materials

journal homepage: www.keaipublishing.com/en/journals/bioactive-materials

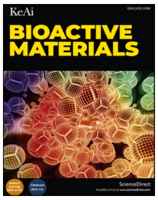

An engineered M2 macrophage-derived exosomes-loaded electrospun biomimetic periosteum promotes cell recruitment, immunoregulation, and angiogenesis in bone regeneration

Zhuohao Wen [a,1], Shuyi Li [a,1], Yi Liu [b,c,d,1], Xueyan Liu [e], Huiguo Qiu [f], Yuejuan Che [g,h,*], Liming Bian [b,c,d,**], Miao Zhou [a,***]

[a] *Department of Stomatology, Guangdong Provincial People's Hospital (Guangdong Academy of Medical Sciences), Southern Medical University, Guangzhou, 510080, China*
[b] *School of Biomedical Sciences and Engineering, Guangzhou International Campus, South China University of Technology, Guangzhou, 511442, China*
[c] *National Engineering Research Center for Tissue Restoration and Reconstruction, South China University of Technology, Guangzhou, 510006, China*
[d] *Guangdong Provincial Key Laboratory of Biomedical Engineering, South China University of Technology, Guangzhou, 510006, China*
[e] *Affiliated Stomatology Hospital of Guangzhou Medical University, Guangdong Engineering Research Center of Oral Restoration and Reconstruction, Guangzhou Key Laboratory of Basic and Applied Research of Oral Regenerative Medicine, Guangzhou, 510182, China*
[f] *Zhuhai Stomatological Hospital, Zhuhai, 519000, China*
[g] *Department of Biomedical Engineering, School of Materials Science and Engineering, South China University of Technology, Guangzhou, 510641, China*
[h] *Department of Anesthesiology, Sun Yat-sen Memorial Hospital, Sun Yat-sen University, Guangzhou, 510120, China*

ARTICLE INFO

Keywords:
Biomimetic periosteum
Engineered exosome
Osteogenic induction
Immune regulation
Bone regeneration

ABSTRACT

The periosteum, a fibrous tissue membrane covering bone surfaces, is critical to osteogenesis and angiogenesis in bone reconstruction. Artificial periostea have been widely developed for bone defect repair, but most of these are lacking of periosteal bioactivity. Herein, a biomimetic periosteum (termed PEC-Apt-NP-Exo) is prepared based on an electrospun membrane combined with engineered exosomes (Exos). The electrospun membrane is fabricated using poly(ε-caprolactone) (core)-periosteal decellularized extracellular matrix (shell) fibers via coaxial electrospinning, to mimic the fibrous structure, mechanical property, and tissue microenvironment of natural periosteum. The engineered Exos derived from M2 macrophages are functionalized by surface modification of bone marrow mesenchymal stem cell (BMSC)-specific aptamers to further enhance cell recruitment, immunoregulation, and angiogenesis in bone healing. The engineered Exos are covalently bonded to the electrospun membrane, to achieve rich loading and long-term effects of Exos. *In vitro* experiments demonstrate that the biomimetic periosteum promotes BMSC migration and osteogenic differentiation via Rap1/PI3K/AKT signaling pathway, and enhances vascular endothelial growth factor secretion from BMSCs to facilitate angiogenesis. *In vivo* studies reveal that the biomimetic periosteum promotes new bone formation in large bone defect repair by inducing M2 macrophage polarization, endogenous BMSC recruitment, osteogenic differentiation, and vascularization. This research provides valuable insights into the development of a multifunctional biomimetic periosteum for bone regeneration.

Peer review under the responsibility of editorial board of Bioactive Materials.

* Corresponding author. Department of Anesthesiology, Sun Yat-sen Memorial Hospital, Sun Yat-sen University, Guangzhou, 510120, China.

** Corresponding author. School of Biomedical Sciences and Engineering, Guangzhou International Campus, South China University of Technology, Guangzhou, 511442, China.

*** Corresponding author. Department of Stomatology, Guangdong Provincial People's Hospital (Guangdong Academy of Medical Sciences), Southern Medical University, Guangzhou, 510080, China.

E-mail addresses: cheyj@mail.sysu.edu.cn (Y. Che), bianlm@scut.edu.cn (L. Bian), zhoumiao@gdph.org.cn (M. Zhou).

[1] These authors contributed equally.

https://doi.org/10.1016/j.bioactmat.2025.03.027
Received 6 December 2024; Received in revised form 4 February 2025; Accepted 27 March 2025

1. Introduction

Periosteum is a connective tissue membrane that envelops most of the surface of bone. Periosteum consists of two layers: an outer fibrous layer and an inner cambium layer, which possesses osteogenic potential [1]. The outer layer of the periosteum is composed of fibroblasts, collagen, and elastin, as well as nerve and microvascular networks, thereby conferring its mechanical stability. The inner layer contains mesenchymal stem cells, osteoblast progenitors, and osteoblasts, all of which are distributed within a sparse collagen matrix that serves as a reservoir for stem cells and growth factors [2]. The process of bone defect healing is complex, and the periosteum plays a crucial role. Cell tracing studies have revealed that nearly 90 % of new bone in the early fracture callus originates from the periosteum [3,4]. When bone tissue is damaged, blood vessels nearby rupture, allowing blood to flow into the defect area and forming a hematoma. Immune cells, predominantly macrophages, mediate the inflammatory response within the defect site. A series of cytokines are secreted to initiate inflammation and promote healing [5]. Initially, macrophages polarize into the M1 type, which secretes various pro-inflammatory cytokines (including tumor necrosis factor-α, interleukin-1, and interleukin-6) to combat infection, promote osteoclast differentiation, and phagocytize bone fragments [6]. Macrophages then transition from M1 to M2 polarization and secrete cytokines (including interleukin-4 and interleukin-10) to resolve inflammation and enhance BMSC activity and osteogenic differentiation [7,8]. The early inflammatory response to bone defects activates the periosteum. The periosteum subsequently thickens, and periosteal cells proliferate. The rich vascular network in the periosteum promotes angiogenesis and ensures the vascularization of the bone. Additionally, the periosteum serves as a scaffold or matrix, promoting the homing of BMSCs to injury sites by secreting stromal cell-derived factor 1 (SDF-1), CXC-chemokine receptor 1 (CXCR1), and periostin (POSTN) [9,10]. BMSCs and osteoblast progenitors in the periosteum induce robust chondrogenesis and osteogenesis, ultimately contributing to bone remodeling [11]. Thus, the periosteum fulfills several critical roles in bone repair: 1) serving as a scaffold or carrier for cells and growth factors; 2) regulating inflammation; 3) recruiting endogenous stem cells; 4) promoting vascularization; and 5) facilitating osteogenesis. However, clinical bone defects are often accompanied by the loss of periosteum. Traditional autologous periosteum transplantation is limited by immune rejection, a shortage of donors, and the complexity of donor surgery. In particular, intramembranous ossification is the primary mechanism that underlies craniofacial bone development. The artificial periosteum currently utilized in oral surgery lacks the essential functions for immunomodulation, vascularization, and osteogenesis. Therefore, the development of a tissue-engineered periosteum with multifunctional properties that mimic the natural periosteum is of great significance for craniofacial bone regeneration.

Poly(ε-caprolactone) (PCL) is extensively utilized in fabricating tissue-engineered periosteum due to its favorable mechanical properties and its approval by the U.S. Food and Drug Administration (FDA). However, PCL exhibits suboptimal cell adhesion properties [12,13]. The periosteal extracellular matrix (ECM) retains the collagen network and the functional components of the periosteum. Biomaterials derived from the decellularized periosteum matrix enhance cell adhesion, proliferation, and osteogenic differentiation [14,15]. In our preliminary studies, a tissue-engineered periosteum with bioactive, periosteum-specific surfaces and tailored physicochemical properties was developed through coaxial electrospinning of PCL and ECM. The PCL/ECM coaxially electrospun membrane (PEC) exhibits a delicate core-shell structure, combining the advantages of ECM and PCL, and possesses suitable stiffness, tensile strength, and degradation rates, thereby providing an optimal environment for the proliferation and mineralization of BMSCs [16]. However, compared to the native periosteum, PEC still lacks adequate capacities for immunomodulation, endogenous cell recruitment, and vascularization promotion.

As key regulators in bone defect healing, macrophages release various cytokines to mediate the recruitment and differentiation of BMSCs and vascular progenitor cells at the fracture site, facilitating angiogenesis and tissue matrix remodeling [17]. M2 macrophages, in particular, release oncostatin M (OSM), bone morphogenetic protein-2 (BMP-2), transforming growth factor-beta (TGF-β), vascular endothelial growth factor (VEGF), and insulin-like growth factor 1 (IGF-1) through paracrine signaling, which plays a pivotal role in stem cell recruitment, ossification, and vascularization [18,19]. Exosomes (Exos) are important mediators of paracrine signaling; they deliver lipids, DNA, non-coding RNA, and proteins derived from host cells, serving as key mediators of communication between macrophages and BMSCs [20]. Numerous studies have demonstrated that M2 macrophage-derived Exos can regulate M2 macrophage polarization in bone defect regions, promote angiogenesis, and accelerate bone healing [21,22]. However, despite exhibiting comparable biological activity to living cells, Exos are difficult to obtain and possess a short half-life, leading to inefficient extraction, rapid accumulation, and inactivation in the liver and spleen upon entering the circulatory system [23]. Therefore, Exos are expected to anchor at the bone defect site and selectively bind to target cells for better regeneration in bone defects [24,25].

Aptamers (Apt) are specialized functional nucleic acids that serve as recognition ligands with high specificity and affinity. These single-stranded oligonucleotides fold into unique tertiary structures for specific recognition and can be conjugated to functional groups and molecular markers through RNA nanotechnology to form multifunctional nanoparticles [26]. Consequently, they are frequently employed in disease diagnosis and targeted therapy [27,28]. Among the various methods employed to construct RNA nanoparticles, the pRNA three-way junction (3WJ) has been widely used as a central scaffold for the construction of multifunctional RNA nanoparticles [29,30]. The branching feature of the 3WJ motif facilitates the convenient incorporation of multiple functional modules into its three helical regions, making it an ideal scaffold for targeted drug delivery [31,32]. Currently, Apt- and 3WJ-based nanoparticles demonstrate significant potential for applications in treatment, imaging, and diagnosis [33,34].

In this study, an engineered Exo-modified biomimetic periosteum (termed PEC-Apt-NP-Exo) was developed for bone regeneration. Amino- and cholesterol-modified BMSC Apts were conjugated to M2 macrophage-derived Exos via the 3WJ platform to create engineered Exos, which were subsequently covalently linked to the ECM shell of PEC membranes, forming a biomimetic periosteum. *In vitro* and *in vivo* experiments confirmed that the biomimetic periosteum exhibited multifunctionality in regulating the immune microenvironment, recruiting endogenous BMSCs, and promoting vascularization and bone regeneration (Scheme 1). This study establishes a novel multifunctional biomimetic periosteum to enhance craniofacial bone healing.

2. Materials and methods

2.1. Synthesis of Apt nanoparticles

A BMSC-specific Apt was obtained based on previous reports and synthesized by Weinabio medicine (Guangdong) Co., Ltd. [35–37]. The sequences of the BMSC-specific Apt and the scrambled control are as follows: Apt, 5′-ACGACGGTGATATGTCAAGGTCGTATGCACGAGTCAGAGG-3′; Scramble, 5′-GAGTATATGTTAGGCCTGGGTGAGTCCTTGCGTCTTCTA-3′.

To verify the specificity of the Apt for BMSCs, mouse BMSCs (Procell, China) were seeded in 15 mm confocal culture dishes and cultured in Dulbecco's modified Eagle medium (DMEM, Gibco, USA) supplemented with 10 % fetal bovine serum (FBS, ExCell, China) and 1 % penicillin-streptomycin (PS, Gibco, USA) at 37 °C under 5 % CO_2. After cell adhesion, they were incubated with 400 nM Alexa Fluor 647 (AF647)-labeled Apt or scrambled sequence at 37 °C for 4 h ($n = 3$), followed by two washes with phosphate-buffered saline (PBS, Gibco, USA). Cells

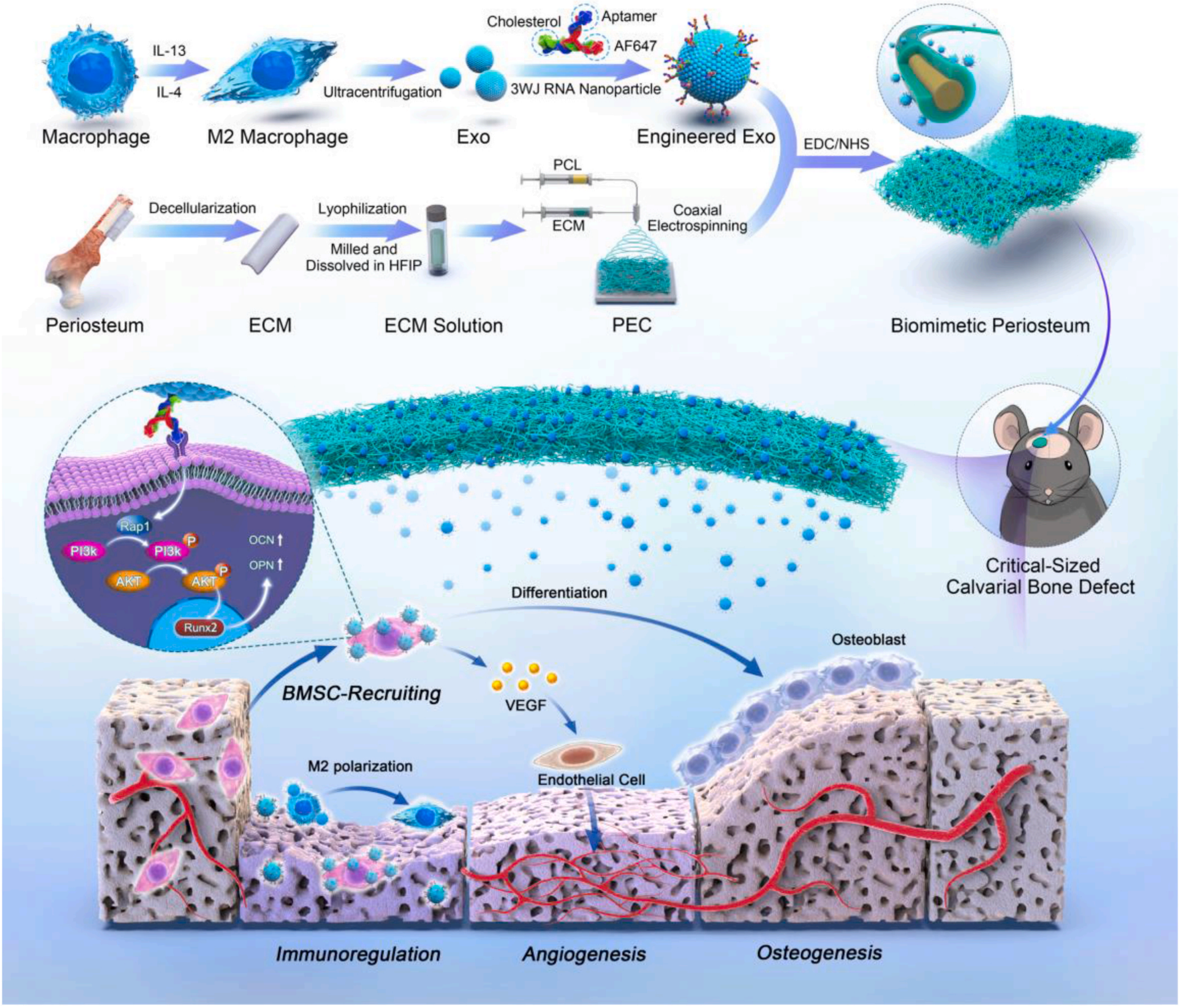

Scheme 1. In this study, a bioactive and biomimetic periosteum (i.e., PEC-Apt-NP-Exo) was constructed by combining the electrospun membrane with engineered Exos: (1) the biomimetic electrospun membrane comprised PCL core-ECM shell fibers created via coaxial electrospinning; (2) the bioactive engineered Exos derived from M2 macrophage were modified with BMSC-specific aptamers; and (3) the engineered Exos were covalently bonded to the electrospun membrane. *In vitro* and *in vivo* results revealed that PEC-Apt-NP-Exo promoted immune regulation, osteogenesis, and angiogenesis through the Rap1/PI3K/AKT signaling pathway, demonstrating significant efficacy in repairing large bone defects.

were then fixed with 4 % paraformaldehyde for 30 min, and the cytoskeleton and nuclei were stained with phalloidin (Beyotime, China) and DAPI staining solutions (Beyotime, China), respectively. Finally, Apt binding to BMSCs was visualized using a confocal microscope (Leica, Germany).

To further verify the binding specificity of the Apt for BMSCs, Raw264.7 cells (Procell, China) were used as controls. A 100 μL suspension of BMSCs or Raw264.7 cells (1×10^7 cells/mL) was incubated with 200 nM Apt or scrambled sequence at 37 °C for 3 h ($n = 3$). The cells were washed twice with PBS, resuspended in 300 μL of flow cytometry staining solution, filtered through a 400-mesh filter, and the Apt binding rate was analyzed by flow cytometry.

After confirming the targeting specificity of the Apt, we designed Apt nanoparticles (Apt-NPs) and nanoparticles (NPs) for subsequent experiments. Apt-NP consists of three single strands: a_{3WJ}-CHOL, b_{3WJ}-Apt-NH_2, and c_{3WJ}-AF647, and NP consists of three single strands: a_{3WJ}-CHOL, b_{3WJ}-NH_2, and c_{3WJ}-AF647. The a_{3WJ}-linked cholesterol can bind to the lipid envelope of Exo. The b_{3WJ}-linked an amino-modified BMSC-specific Apt for Apt-NPs or an amino group for NPs can bind to the carboxyl groups of ECM on PEC surface via EDC/NHS reaction. The c_{3WJ}-linked AF647 provides fluorescent labeling for tracing. All the RNA oligos were synthesized by Weinabio medicine (Guangdong) Co., Ltd., and their sequences are listed as follows: a_{3WJ}-CHOL, 5′- UUGCCAUGUGUAUGUGGG-CHOL-3’; b_{3WJ}-Apt-NH_2, 5′-CCCACAUACUUUGUUGAUCCACGACGGTGATATGTCAAGGTCGTATGCACGAGTCAGAGG-NH_2-3’ (underlined portions indicate Apt sequences); b_{3WJ}-NH_2, 5′-CCCACAUACUUUGUUGAUCC-NH_2-3’; c_{3WJ}-AF647, 5′-GGA UCA AUC AUG GCA A-AF 647-3’. The functionalized a_{3WJ}, b_{3WJ}, and c_{3WJ} strands were mixed at a 1:1:1 M ratio and self-assembled through annealing in a PCR instrument at 95 °C for 5 min, followed by gradual cooling at a rate of 0.5 °C/s to 4 °C. The assembled Apt-NPs and NPs were characterized by polyacrylamide gel electrophoresis (PAGE).

2.2. Isolation, culture, and identification of M2 macrophages

Mouse bone marrow-derived cells (BMDCs) were first extracted. The tibia and femur were isolated from healthy 6-week-old male C57BL/6J mice, and the muscle tissue was removed under sterile conditions to expose the bone marrow cavity. The bone marrow was flushed into pre-cooled PBS, filtered through a 70 μm filter, and centrifuged at 500 g for 5 min. The supernatant was discarded. Three volumes of Tris-NH_4Cl red blood cell lysis buffer (Leagene, China) were added to the cell pellet, lysed on ice for 2 min, then centrifuged and washed. The extracted BMDCs were cultured in DMEM supplemented with 10 % FBS, 100 U/mL PS, and 20 ng/mL macrophage colony-stimulating factor (M-CSF, Peprotech, USA). Mature BMDMs were obtained on day 7. To induce M2 macrophages, 10 ng/mL interleukin-4 (IL-4, Peprotech, USA) and 10 ng/mL interleukin-13 (IL-13, Peprotech, USA) were added to the culture medium and incubated for 24 h.

To identify M2 macrophages, the induced cells were resuspended in a Cell Staining Buffer, incubated with Fc receptor blocking solution (Biolegend, USA), and labeled with FITC-conjugated anti-mouse F4/80 (Biolegend, USA). An equal amount of isotype control antibody was added to the control group, incubated, and washed. The cells were fixed and permeabilized using intracellular fixation and permeabilization buffer (eBioscience, USA), followed by staining with APC-conjugated anti-mouse CD206 (Biolegend, USA). The control group received an equal amount of isotype control antibody, and M2 macrophages were identified and analyzed by flow cytometry ($n = 3$).

2.3. Isolation and characterization of Exos

First, FBS was ultracentrifuged at 120,000 g for 16 h at 4 °C to remove Exos. The medium was then prepared using Exo-free FBS, and M2 macrophages were cultured accordingly. After 48 h, the cell supernatant was collected and centrifuged at 2000 g for 20 min, followed by 10,000 g for 5 min, and concentrated by centrifugation at 4000*g* for 20 min using a 100 kDa filter (MerckMillipore, Germany). The concentrated supernatant was transferred to an XPN-100 ultracentrifuge (Beckman, USA) and centrifuged at 150,000 g for 90 min. Following centrifugation, the precipitate was washed with PBS, filtered through a 0.22 μm filter, and centrifuged again. The Exo pellet was resuspended in sterile PBS and stored at −80 °C for subsequent experiments.

The Exo protein concentration was quantified using a bicinchoninic acid (BCA) protein assay kit (Beyotime, China). To observe Exo uptake by BMSCs, Exos were labeled with DiO staining solution (Beyotime, China) and incubated for 20 min. Excess dye was removed using a 100 kDa ultrafiltration tube and two washes. DiO-labeled Exos (100 μg/mL) were incubated with BMSCs at 37 °C for 4 h. The cell nuclei were stained with DAPI, and the uptake of Exos was observed and imaged using a confocal microscope. Exo surface markers, including TSG101, Flotillin-1, Calreticulin, and Alix (Proteintech, China), were detected by Western blotting (WB).

2.4. Conjugation of Apt-NPs to Exos and characterization

To combine Apt-NPs with Exos and form engineered Exos (Apt-NP-Exos), 100 μg of Exos were resuspended in 0.56 nmol of Apt-NPs and incubated at 37 °C for 45 min. The mixture was then transferred to ice for incubation for 1 h. Unbound Apt-NPs were removed using a 100 kDa ultrafiltration tube, followed by two PBS washes. The binding rate and particle size of Apt-NPs and Exos were measured using a nanoflow cytometer (NanoFCM, China), while markers and morphology before and after binding were analyzed by WB and transmission electron microscopy (TEM, JEOL, Japan).

2.5. Biological Effects of Apt-NP-Exos on BMSCs

To assess the affinity of BMSCs for Apt-NP-Exos, mouse BMSCs were incubated with 100 μg/mL DiO-labeled Exos, NP-Exos, or Apt-NP-Exos for 4 h ($n = 6$). Confocal microscopy was used to visualize the internalization of Exos by BMSCs from different treatment groups, and fluorescence intensity was quantified using the ImageJ software.

The effect of Apt-NP-Exos on BMSCs proliferation was evaluated using the Cell Counting Kit-8 (CCK-8) proliferation assay. BMSCs were seeded in 96-well plates. After adherence, the medium was replaced with serum-free medium containing 0 μg/mL, 25 μg/mL, 50 μg/mL, or 100 μg/mL suspension of Apt-NP-Exos ($n = 6$), and the cells were cultured in an incubator (37 °C, 5 % CO_2) for 24 and 48 h. At the indicated time points, 10 μL of CCK-8 solution (Beyotime, China) was added to each well and incubated for 2 h, followed by measurement of the OD value at 450 nm using a microplate reader (Thermo Fisher Scientific, USA).

To investigate the effect of Apt-NP-Exos on the osteogenic differentiation of BMSCs, mouse BMSCs were seeded in 48-well plates and cultured with medium containing 100 μg/mL of Exos or Apt-NP-Exos, while the control group received an equal volume of PBS ($n = 3$). The relevant assays were conducted at specified time points. After 7 days of culture, the expression of osteogenic-related proteins was analyzed by WB. Briefly, the cells were lysed with RIPA lysis buffer (Beyotime, China), and after a 10-min incubation in a 95 °C water bath, proteins were separated by SDS-PAGE and transferred to a polyvinylidene fluoride (PVDF) membrane. The membrane was blocked with blocking buffer (Beyotime, China) for 15 min, followed by incubation with anti-Runx2, anti-BMP2, and anti-GAPDH antibodies (Proteintech, China) overnight at 4 °C. The secondary antibody was incubated on a shaker at room temperature for 1 h. Protein expression levels were detected using the Odyssey CLx imaging system (Biosciences, USA), and protein band density was semi-quantified using ImageJ software. At the same time point, alkaline phosphatase (ALP) staining was performed using BCIP/NBT solution (Beyotime, China) and observed under an optical microscope. Cells were lysed using cell lysis buffer, and the protein concentration of the lysate was determined using the BCA method. ALP activity was detected and calculated using an alkaline phosphatase detection kit (Beyotime, China). After 14 days of culture, alizarin red staining was performed to observe the formation of mineralized matrix under an optical microscope. Subsequently, 100 mM dodecylpyridinium chloride solution was added to each well, and the absorbance at 562 nm was measured using a microplate reader to quantify mineralized matrix content.

2.6. Preparation and characterization of PEC-Apt-NP-Exos

Fresh pig femurs were collected from slaughterhouses, and the periosteum was isolated after removing soft tissues like muscles and fascia. Under sterile conditions, the periosteum was washed with ultrapure water, treated with 1 % Triton X-100, and shaken at room temperature for 10 h. It was then washed three times with ultrapure water, followed by treatment with 1 % sodium dodecyl sulfate (SDS) for 2 h, and then washed three additional times with ultrapure water. The sample was treated with 100 U/mL DNase overnight in a 37 °C water bath, then washed three times with ultrapure water. To assess the decellularization efficiency, the decellularized periosteum was fixed, dehydrated, paraffin-embedded, and sectioned. The tissue structure and cellular components were observed using DAPI, hematoxylin and eosin (HE), and Masson staining. Genomic DNA from the decellularized periosteum was extracted, analyzed by agarose gel electrophoresis, and quantified using the Quant-iT PicoGreen dsDNA kit (Invitrogen, USA) ($n = 3$).

The decellularized periosteum was freeze-dried, chopped, ground, and sieved to produce a powder with a particle size of less than 425 μm. 500 mg of decellularized periosteum powder was added to 10 mL of hexafluoroisopropanol (HFIP, Aladdin, China) and stirred magnetically at 4 °C until completely dissolved into a 5 % (w/v) ECM shell solution. PCL particles were dissolved in HFIP to a final concentration of 12 % (w/

v). These solutions were then loaded into syringes and attached to syringe pumps. The flow rates of the PCL and ECM solutions were set to 1 mL/h and 2.5 mL/h, respectively. Using ECM as the shell and PCL as the core, electrospinning was performed at 12.9 kV through a coaxial spinning nozzle (outer: 16 G, inner: 22 G). The electrospun membranes were soaked in 75 % ethanol for 3 h, followed by UV sterilization for 4 h, before subsequent experiments.

To couple Apt-NP-Exos to PEC, an EDC/NHS-catalyzed amidation reaction was performed under sterile conditions. First, 100 mL of MES buffer was prepared, and EDC, NHS, and PEC were added sequentially in a mass ratio of 5:2:1. The reaction proceeded at room temperature for 2 h to activate the carboxyl groups of ECM, followed by two washes with PBS. The activated PEC was immersed in 100 μg/mL suspension of Apt-NP-Exos and incubated on a shaker at 4 °C for 12 h, allowing the amino groups in Apt-NP-Exos to bind with the carboxyl groups in PEC. Uncoupled Apt-NP-Exos or Exos were removed by two washes with PBS. A control group without EDC/NHS catalysis was treated using the same procedure. The loading efficiency of Apt-NP-Exos was evaluated using confocal microscopy, and fluorescence intensity was quantified with ImageJ software ($n = 5$). Additionally, PEC-Apt-NP-Exos were placed at the bottom of a 24-well plate, 500 μL of PBS was added to each well, and incubated at 4 °C in the dark. PBS was collected and replaced every 24 h. On day 7, the collected PBS was analyzed using a fluorescence microplate reader to measure the fluorescence intensity of AF647 ($n = 3$).

Live/dead staining was performed to assess the effect of PEC-Apt-NP-Exos on BMSC proliferation. PCL, PEC, and PEC-Apt-NP-Exo membranes were fixed at the bottom of a 24-well plate, and BMSCs were seeded ($n = 3$). After 72 h of culture, the medium was removed, and the cells were washed with PBS. Then, 300 μL of Calcein AM/PI solution was added to each well and incubated at 37 °C in the dark for 30 min. The staining results were observed under a fluorescence microscope. Additionally, CCK-8 analysis was performed using the same procedure ($n = 6$).

To investigate the effect of PEC-Apt-NP-Exo on BMSC osteogenic differentiation, BMSCs were seeded on PCL, PEC, and PEC-Apt-NP-Exo membranes ($n = 3$). ALP staining, ALP activity detection, and WB assays were conducted after 7 days of culture, while Alizarin Red S (ARS) staining and quantification were performed after 14 days of culture, following the same procedures as before.

2.7. *PEC-Apt-NP-Exos recruiting BMSCs*

A Transwell chemotaxis assay was used to evaluate the chemotactic effect of PEC-Apt-NP-Exos on BMSCs *in vitro*. To clarify the effective components of PEC-Apt-NP-Exos, the following experiments were conducted across six groups: 1) Blank group: no materials were used; 2) PCL group; 3) PEC group; 4) PEC-Exo group: PEC was physically loaded by soaking in PBS solution containing 100 μg/mL of Exos; 5) PEC-NP-Exo group: Exos were chemically connected to PEC via 3WJ nanoparticles using amide condensation; and 6) PEC-Apt-NP-Exo group: engineered Exos modified with BMSC-specific Apts were chemically connected to PEC (Fig. S1). Membranes from each group were fixed to the bottom of the Transwell chamber ($n = 3$). Then, BMSCs were seeded into the upper chambers and cultured in DMEM supplemented with 1 % FBS and 1 % PS. 600 μL of standard DMEM was added to the lower chamber. After 24 h of incubation, non-migrating cells in the upper chamber were scraped away. The migrated cells on the underside of the upper chamber membrane were fixed in 4 % paraformaldehyde. Cells were stained with 0.1 % crystal violet (Beyotime, China) for 20 min. Migrated cells were imaged using an optical microscope and counted with ImageJ software.

2.8. *In vitro vascularization assay*

To investigate the effect of Exos on the crosstalk between BMSCs and endothelial cells, BMSCs were cultured in a medium with or without 100 μg/mL suspension of Exos ($n = 3$). The supernatants were collected after 24 h and labeled SN_{Exo} and SN, respectively (Fig. 6A). The VEGF levels in SN_{Exo} and SN were measured using enzyme-linked immunosorbent assay (ELISA) kits (Elabscience, China), according to the manufacturer's protocol.

Mouse endothelial cells (bEND.3) were cultured in 6-well plates with 2 mL of either SN_{Exo} or SN. Control groups were cultured in a medium with or without 100 μg/mL suspension of Exos (Exo group and DMEM group, respectively) ($n = 3$). After 24 h of culture, bEND.3 cells were reseeded onto Matrigel-coated 96-well plates and cultured for 4 h. Cells were stained with calcein-AM at 37 °C for 15 min. Plates were then observed and photographed under a fluorescence microscope, and the results were quantified using the AngioTool software.

To explore the effect of PEC-Apt-NP-Exos on the crosstalk between BMSCs and bEND.3, BMSCs were seeded and cultured on PCL, PEC, and PEC-Apt-NP-Exo membranes, and the supernatants were collected. The same experimental procedure described above was followed ($n = 3$).

2.9. *Animal experiments*

All procedures were conducted in accordance with the Guidelines for the Care and Use of Laboratory Animals of the Guangdong Academy of Medical Sciences and approved by the Ethics Committee for Animal Experiments (No. KY2023-584-01). A cranial defect model using male C57 mice (6-week-old, 20–25 g) was employed to evaluate the recruitment of endogenous cells, vascularization, and osteogenesis induced by PEC-Apt-NP-Exos. Prior to surgery, the skull hair was removed, and the skin was sterilized after general anesthesia was induced via intraperitoneal injection of sodium pentobarbital. A midline incision was made, and the soft tissue was bluntly dissected to fully expose the surgical site. The periosteum was removed, and critical-sized bone defects (4-mm diameter) were created on the right side using a trephine drill. Based on the experimental groups, PCL, PEC, PEC-Exo, PEC-NP-Exo, or PEC-Apt-NP-Exo membranes were applied to the defect areas, and the wound was closed in layers with strict adherence to closure protocols (Fig. S2).

Animals from each group were euthanized with isoflurane at 1, 4, and 8 of weeks after implantation ($n = 6$ per group). The harvested calvarial specimens were fixed in 10 % neutral buffered formalin for 48 h before radiographic and histological examinations.

2.10. *Immunofluorescence*

The calvarial specimens were decalcified in 10 % EDTA solution at 37 °C for 4 weeks. The samples were then dehydrated in graded ethanol solutions and embedded in paraffin. Paraffin sections approximately 4-μm thick were prepared using a Leica RM2016 microtome. Immunofluorescence double staining was performed to identify M1 and M2 macrophages. Tissue sections were incubated overnight at 4 °C with primary antibodies against CD68, CD80, and CD206 (ServiceBio, China). Sections were then incubated with secondary donkey anti-rabbit IgG antibodies conjugated to horseradish peroxidase (Abcam, England), and nuclei were counterstained with DAPI for 10 min. Stained sections were observed and imaged using a fluorescence microscope. M1 macrophages (CD68-positive and CD80-positive) and M2 macrophages (CD68-positive and CD206-positive) were counted in five randomly selected merged microscopic images per group, with blind evaluations performed twice by two independent assessors.

SSEA4 (Santa, USA) and CD45 (ServiceBio, China) immunofluorescence staining were conducted using the same procedure, with BMSCs defined as SSEA4-positive and CD45-negative.

2.11. *Immunohistochemistry*

The sections were stained with HE and Masson trichrome to assess new bone formation. To analyze the angiogenic and osteogenic activity of the samples, paraffin sections were dewaxed and hydrated using xylene and graded alcohols. Tissue sections were then placed in a repair cassette filled with citric acid antigen retrieval buffer (pH 6.0) and heated in a microwave for antigen retrieval. After blocking with goat-derived rabbit serum, tissue sections were incubated overnight at 4 °C with primary antibodies against CD31 (ServiceBio, China), osteopontin (OPN, ServiceBio, China), and osteocalcin (OCN, ServiceBio, China). The sections were washed three times with PBS, followed by incubation with secondary antibodies for 50 min at room temperature. The color was developed using a diaminobenzidine (DAB) solution, and nuclei were counterstained with hematoxylin. Stained histological sections were imaged using an optical microscope and analyzed with ImageJ software.

2.12. *Micro-computed tomography (micro-CT) analysis*

Radiographic raw data of the calvarial specimens were acquired using micro-CT (SkyScan, Belgium). The scanning parameters were an aluminum filter with 0.5 mm thickness, a spatial resolution of 2000 × 1332, and a pixel size of 9 μm. The acquired data were reconstructed using CTVox software and analyzed with CTAn software after selecting the regions of interest (ROI) in Dataviewer. Bone volume (BV), bone volume fraction (BV/TV), bone surface to tissue volume ratio (BS/TV), and trabecular number (Tb.N) were recorded and calculated (grey threshold: 70–255).

2.13. *Transcriptome sequencing and bioinformatics analysis*

To identify the differential expression of RNA transcripts between PEC and PEC-Apt-NP-Exo groups, genome-wide transcriptional sequencing was performed by Wuhan Benagen Co., Ltd. Differential expression analysis between PEC and PEC-Apt-NP-Exo groups was conducted using the DESeq2 R package ($n = 3$). Gene expression levels were considered statistically significant with a P value < 0.05, as determined by DESeq2. Kyoto Encyclopedia of Genes and Genomes (KEGG) pathway enrichment analysis and Gene Ontology (GO) enrichment analysis were also conducted.

To investigate the activation of signaling pathways, BMSCs were seeded on PEC and PEC-Apt-NP-Exos and cultured for 7 days ($n = 3$). The expressions of Rap1, p-PI3K, PI3K, p-AKT, AKT, and GAPDH were detected via WB assay, following the same protocol as previously described.

2.14. *Statistical analysis*

All experimental data were expressed as mean ± standard deviation and statistically analyzed using GraphPad Prism software. Statistical comparisons between two groups were performed using Student's t-test. Statistical significance among three or more groups was determined using a one-way analysis of variance (ANOVA) followed by the Tukey's post-hoc test. Statistical significance was indicated as $^{***}P < 0.001$, $^{**}P < 0.01$, and $^{*}P < 0.05$.

3. Results

3.1. *Construction of Apt-NP-Exos*

The binding of the BMSC-specific Apt to BMSCs was assessed using confocal microscopy and flow cytometry. After incubating the Apt with BMSCs, a significant amount of red fluorescent-labeled Apt was observed to aggregate in the cells, whereas minimal aggregation was noted in the scramble group (Fig. 1A). Flow cytometry analysis revealed that the binding of BMSCs to the Apt (73.3 %) was significantly higher than in the scramble group (18.8 %), while Raw264.7 showed similar binding to the Apt (6.37 %) and the scramble (5.37 %), indicating the Apts specificity for BMSCs (Fig. 1B).

Apt-NPs were designed for Exo engineering via the 3WJ structure, with NP without Apt used as controls. Apt-NPs and NPs were imaged using PAGE electrophoresis, and no byproduct bands were detected (Fig. S3), indicating that the synthesized nanoparticles were successfully assembled.

The expression of M2 macrophage markers was evaluated using flow cytometry. The results demonstrated that bone marrow-derived macrophages (BMDMs) cultured under induction conditions highly expressed F4/80 and CD206 (99.6 %), confirming successful induction of M2 macrophages (Fig. 1C). Exos were then extracted from M2 macrophages, and their uptake by BMSCs was observed (Fig. 1D). WB analysis revealed enrichment of typical exosomal protein markers, including TSG101, Flotillin 1, and Alix, in the Exos, while the endoplasmic reticulum-specific protein calreticulin was absent, confirming successful Exo isolation (Fig. 1E).

Following the attachment of Apt-NP to Exos, nanoflow cytometry demonstrated a binding rate of 60.1 % (Fig. 1F). Both Apt-NP-Exo and Exo groups expressed exosomal markers (Fig. 1G) and exhibited diameters ranging from 40 to 150 nm (Fig. 1H). They also displayed the typical cup-shaped morphology and double-layer membrane structure (Fig. 1I), consistent with the known characteristics of Exos, confirming the successful construction of engineered Exos.

3.2. *Apt-NP-Exos promoting the proliferation and osteogenic differentiation of BMSCs*

The binding of Exo, NP-Exo, and Apt-NP-Exo to BMSCs was evaluated using confocal microscopy. After incubation with BMSCs, the red fluorescence intensity of the Apt-NP-Exo group (59.13 ± 12.32) was significantly higher than that of the NP-Exo group (13.88 ± 2.58), and the green fluorescence intensity of the Apt-NP-Exo group (114.46 ± 26.19) was also higher than that of the NP-Exo group (57.87 ± 12.67) and the Exo group (65.85 ± 11.72). These results indicated that the engineered Exos had a greater affinity for BMSCs than for Exos and enhanced Exo enrichment in cells, which was mediated by the Apt (Fig. 2A and B).

In the cell activity assay, CCK-8 analysis revealed an increase in OD value over time and with the concentration of Apt-NP-Exos, indicating that Apt-NP-Exos promotes the proliferation of BMSCs. 100 μg/mL suspension of Apt-NP-Exos significantly enhanced BMSCs proliferation, and this concentration was used for subsequent experiments (Fig. 2C).

Osteogenic activity was assessed using ALP staining, ALP activity assays, ARS staining, and WB assay. The results demonstrated that Apt-NP-Exo group exhibited higher ALP activity ($P < 0.001$), while ARS staining and quantification indicated greater mineral deposition compared to the control group ($P < 0.01$), with no significant difference observed compared to the Exo group (Fig. 2D–F). Runx2, a key transcription factor regulating the osteogenic differentiation of BMSCs, and BMP-2, an initial factor for fracture healing, were assessed via WB analysis [38,39]. The Apt-NP-Exo group exhibited significantly higher expression levels of Runx2 ($P < 0.01$) and BMP-2 ($P < 0.001$) compared to the control group, although no significant difference was observed compared to the Exo group (Fig. 2G and H). These findings indicate that engineered Exos promote the osteogenic differentiation of BMSCs and that the modification process does not alter the original osteogenic properties of Exos.

3.3. *Characterization of PEC-Apt-NP-Exos*

PEC was prepared via coaxial electrospinning of PCL (core) and ECM (shell) as shown in Fig. 3A, according to our previous study [16]. Histological staining following periosteum decellularization confirmed the removal of nuclear components, while the periosteal ECM retained its collagen content and exhibited a loose, porous structure (Fig. 3B). Agarose gel electrophoresis revealed no significant DNA residue in the periosteal ECM group (Fig. 3C). The DNA content of the periosteal ECM group decreased from 486.40 ± 92.09 to 16.32 ± 9.56 ng/mg dry weight compared to the femoral periosteum group, meeting the FDA standards for decellularized tissue (Fig. 3D). The mechanical properties

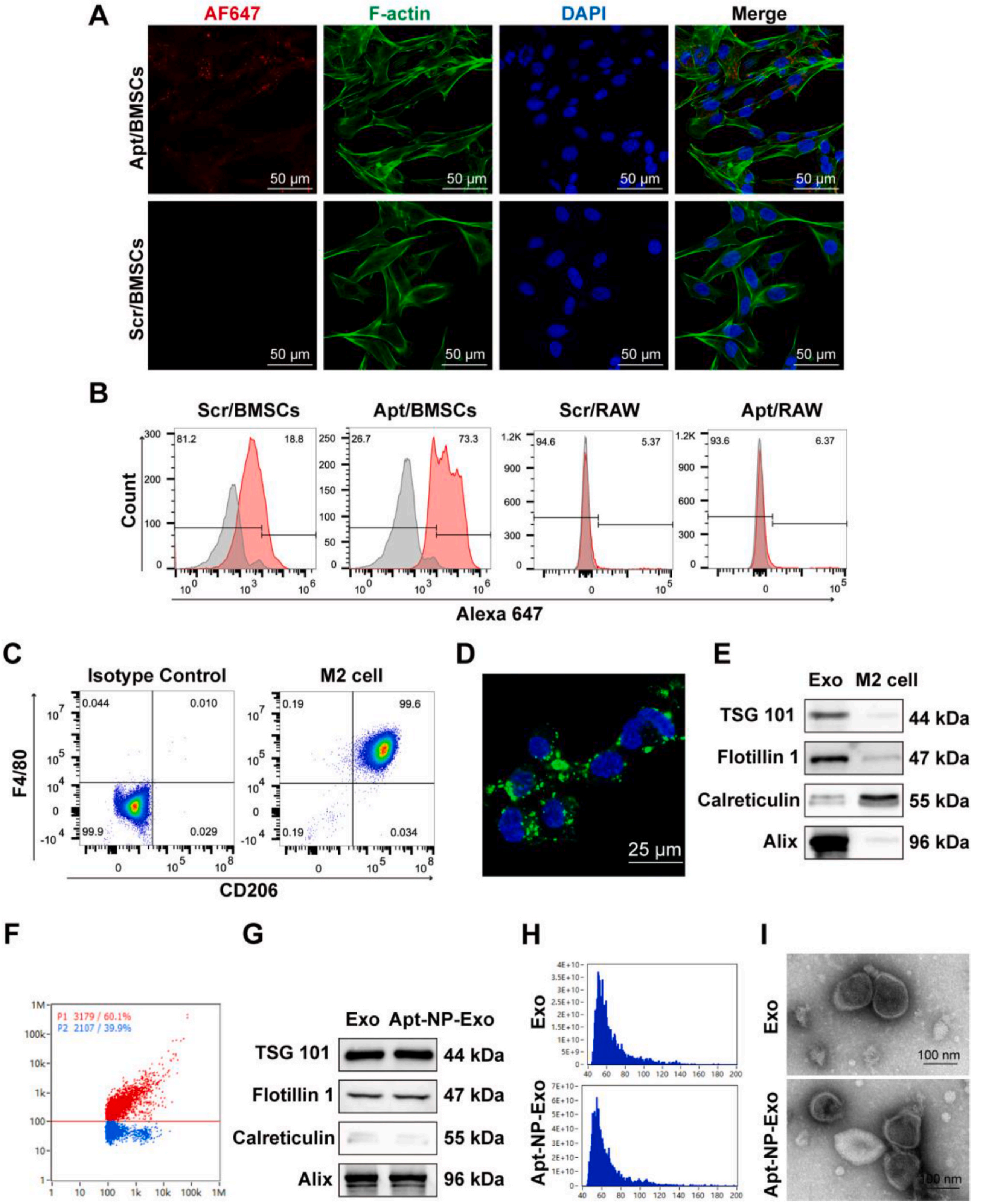

Fig. 1. Construction of Engineered Exos. (A) Representative confocal microscopic images of BMSC Apts after co-culture with BMSCs for 4 h. Red: AF647-labeled Apt; green: F-actin; blue: DAPI-labeled cell nuclei. (B) Flow cytometry analysis was performed to detect the specificity of AF647-labeled BMSC Apts. (C) Flow cytometry analysis of M2 macrophage markers F4/80 and CD206. (D) Confocal microscopic image of DiO-labeled Exos cocultured with BMSCs. (E) WB analysis of exosomal positive and negative markers in Exos and donor cells. (F) Nanoflow cytometry analysis of the binding of Apt nanoparticles to Exos. (G) WB analysis of exosomal positive and negative markers in Exo and Apt-NP-Exo groups. (H) Nanoflow cytometry analysis of size distribution of Exos and Apt-NP-Exos. (I) TEM images of Exos and Apt-NP-Exos.

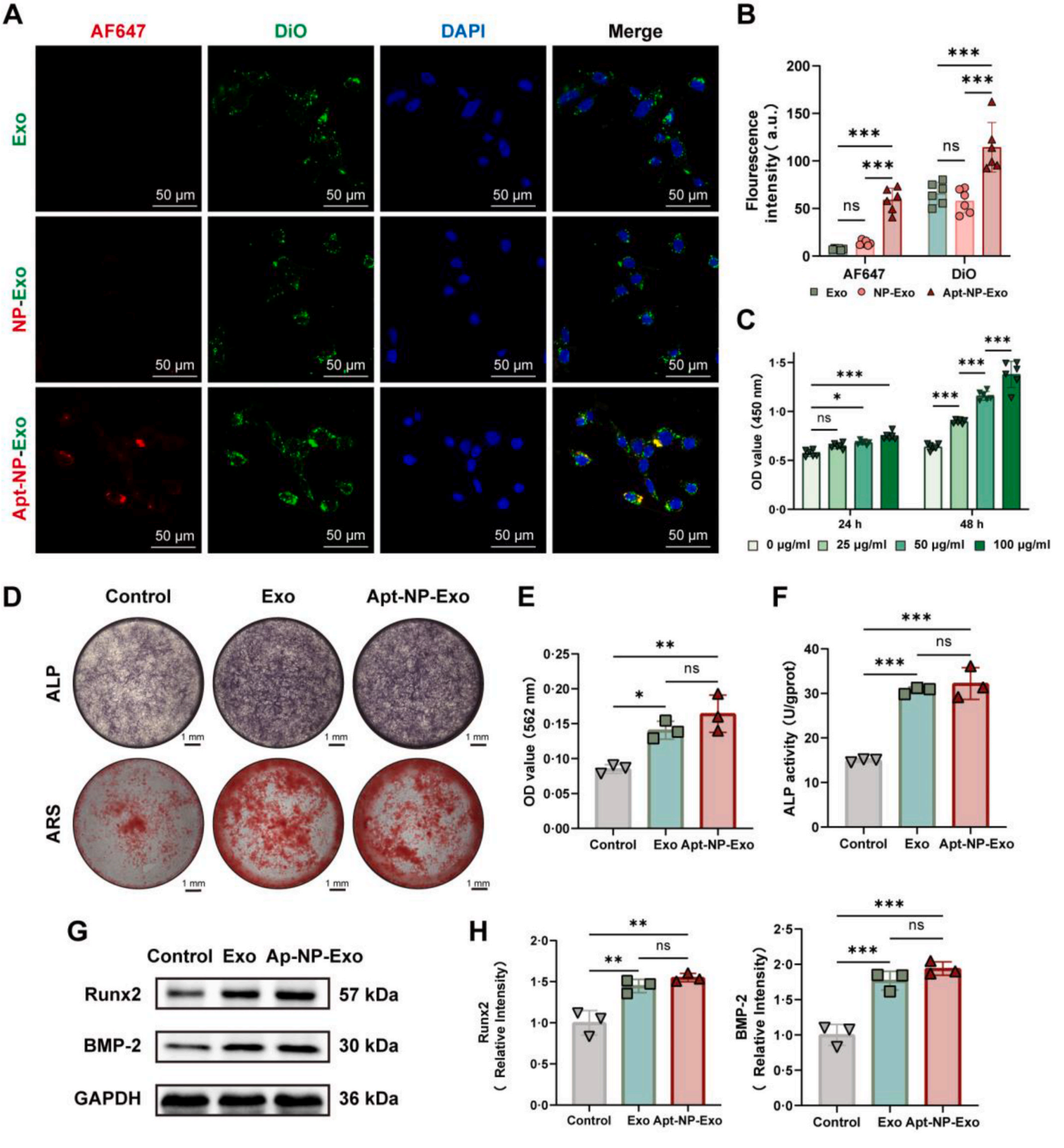

Fig. 2. Biological Effects of Engineered Exos on BMSCs. (A) Representative confocal microscopic images and (B) quantitative analysis showed the internalization of Exos, NP-Exos, and Apt-NP-Exos after culture with BMSCs for 4 h. Red: AF647-labeled NP or Apt-NP; green: DiO-labeled Exos; blue: DAPI-labeled cell nuclei. (C) CCK-8 assay was conducted to evaluate the proliferation of BMSCs treated with different concentrations of Apt-NP-Exo at 24 and 48 h. (D) ALP staining of BMSCs on day 7 and ARS staining on day 14. (E) Quantification of ARS staining. (F) ALP activity of BMSCs on day 7. (G) WB assay and (H) quantitative analysis of Runx2 and BMP-2 expression in BMSCs. Data were shown as mean ± SDs. ns, no significance, ***$P < 0.001$, **$P < 0.01$, *$P < 0.05$.

of PEC were evaluated based on Young's modulus. The results indicated that Young's modulus of the PEC group was significantly higher than that of the ECM group ($P < 0.001$), indicating that PCL incorporation improves the mechanical strength of PEC (Fig. S4).

Apt-NP-Exos were conjugated to PEC via an EDC/NHS-catalyzed amide condensation reaction. Confocal microscopy demonstrated that the loading of Apt-NP-Exos increased significantly following the EDC/NHS reaction (from 514.20 ± 229.20 to 1990.00 ± 484.70) (Fig. 3E and F). Under high magnification, red-labeled Apt-NP-Exos were observed bound to the ECM shell of PEC, displaying a core-shell structure (Fig. 3G). The release characteristics of engineered Exos from PEC-Apt-NP-Exo membranes are illustrated in Fig. 3H. The control group, without

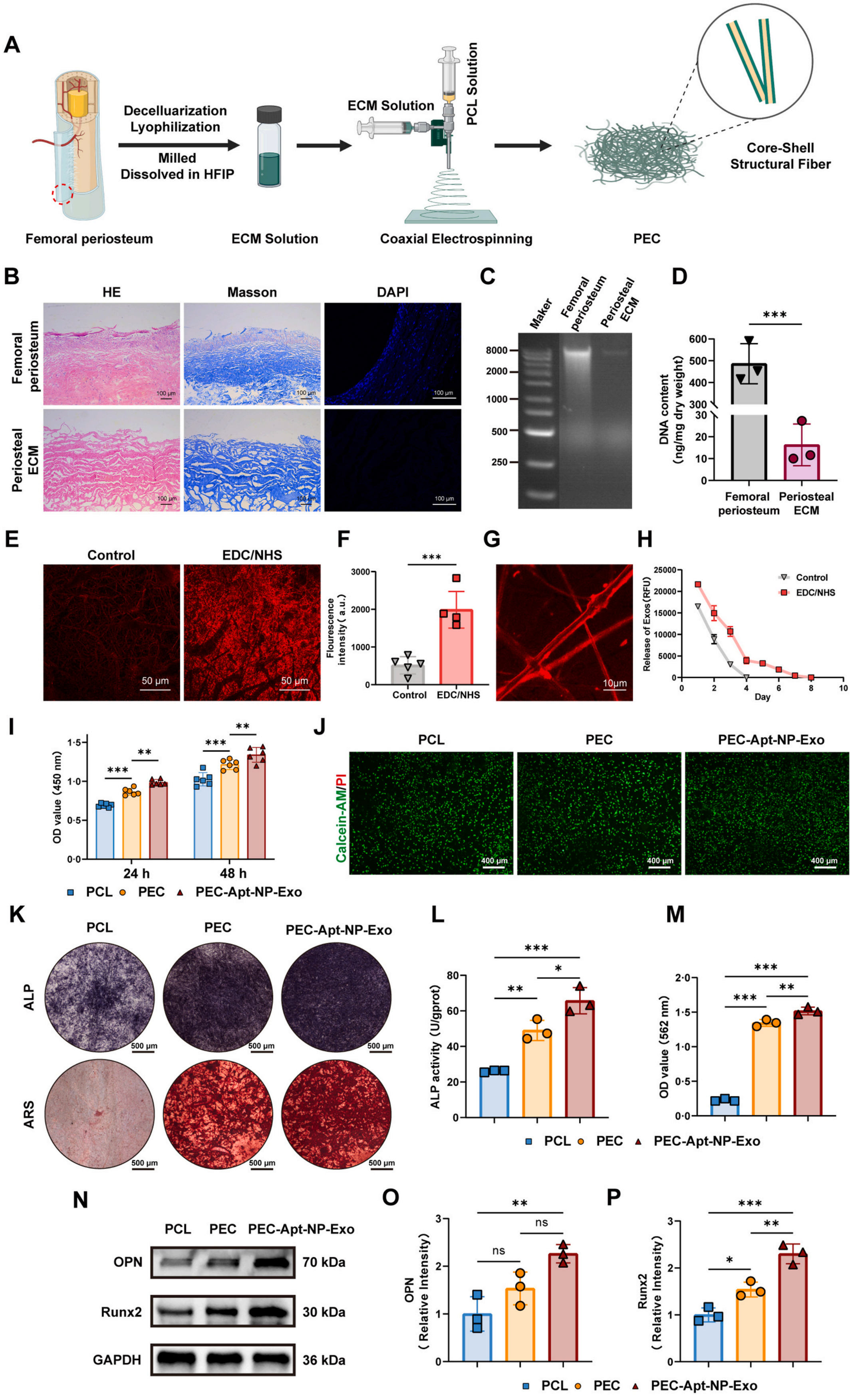

(caption on next page)

Fig. 3. Preparation of PEC-Apt-NP-Exo and Its Effect on Osteogenic Differentiation of BMSCs. (A) Schematic diagram illustrating the preparation of PEC. (B) Comparative study of femoral periosteum and periosteal ECM through HE, Masson, and DAPI staining analysis. (C) Agarose gel electrophoresis and (D) quantification of DNA content in femoral periosteum and periosteal ECM. (E) Confocal microscopy images and (F) quantification were utilized to evaluate the effectiveness of EDC/NHS in coating engineered Exos onto PECs via catalyzed amide condensation reactions. (G) Confocal microscopy images of core-shell structures. (H) Fluorescence microplate reader assay to evaluate the sustained release of engineered Exos. (I) CCK-8 assay and (J) live-dead staining were conducted to evaluate the effect of various membranes on BMSC growth. Green: calcein-AM, living cells; red: PI, dead cells (K) ALP staining of BMSCs on day 7 and ARS staining on day 14. (L) ALP activity of BMSCs on day 7. (M) Quantification of ARS staining. (N) WB assay and (O, P) quantitative analysis of Runx2 and OPN expression in BMSCs. Data were shown as mean ± SDs. ns, no significance, $^{***}P < 0.001$, $^{**}P < 0.01$, $^{*}P < 0.05$.

EDC/NHS reaction for conjugation of Apt-NP-Exos on PEC, rapidly released Apt-NP-Exos within 4 days. In contrast, the PEC-Apt-NP-Exo group, with EDC/NHS reaction for conjugation of Apt-NP-Exos on PEC, showed relatively rapid release of Apt-NP-Exos during the first 3 days, followed by a slower release of Apt-NP-Exos over days 4–8. Meanwhile, the PEC-Apt-NP-Exo group showed higher initial Exo content than the control group. These indicated that PEC-Apt-NP-Exo membrane is capable of effectively loading and slowly releasing engineered Exos. In addition, TEM was employed to observe the engineered Exos released from PEC-Apt-NP-Exo on days 1, 3, 5, and 7. The results demonstrated that the engineered Exos consistently retained their characteristic cup-shaped morphology across all time points, indicating structural stability after release (Fig. S5).

3.4. PEC-Apt-NP-Exos promoting the proliferation and osteogenic differentiation of BMSCs

The cytocompatibility of PEC-Apt-NP-Exo membrane was evaluated using the CCK-8 assay and live/dead staining. Results indicated that PEC-Apt-NP-Exo group significantly enhanced cell proliferation compared to PCL group ($P < 0.001$) and PEC group ($P < 0.01$) (Fig. 3I). Live/dead staining revealed predominantly green-stained living cells on the membrane surfaces across the three groups, with few red dead cells (Fig. 3J), suggesting that PEC-Apt-NP-Exo membranes possess sufficient compatibility and promote BMSC proliferation.

An *in vivo* biosafety analysis was also conducted. Histological staining of major organs (heart, liver, spleen, lung, and kidney) 8-week post-implantation of PEC-Apt-NP-Exo membranes showed healthy tissue, and no abnormalities were detected in routine blood tests, renal function tests, or liver function tests, confirming the biocompatibility of PEC-Apt-NP-Exo membranes *in vivo* (Fig. S6).

Osteogenic activity was assessed using ALP staining, ALP activity assays, ARS staining, and WB assay. ALP staining and activity assays revealed that PEC-Apt-NP-Exo group (65.70 ± 7.41 U/gprot) exhibited higher ALP expression compared to PEC group (49.02 ± 5.69 U/gprot, $P < 0.05$) and PCL group (26.10 ± 0.60 U/gprot, $P < 0.001$). The ALP activity in the PEC group was higher than that in the PCL group ($P < 0.01$). Additionally, ARS staining demonstrated more mineralized nodules in PEC-Apt-NP-Exo group than in PEC and PCL groups (Fig. 3K–M). OPN, a secretory protein produced by osteoblasts, plays a key role in bone repair [40]. WB assay showed higher expression of Runx2 and OPN in PEC-Apt-NP-Exo group compared to PEC and PCL groups (Fig. 3N–P). These findings indicate that PEC-Apt-NP-Exo membrane promotes osteogenic differentiation *in vitro*.

3.5. BMSCs recruitment with PEC-Apt-NP-Exos

The migration of BMSCs was assessed *in vitro* using the Transwell assay. PEC-Apt-NP-Exo group exhibited the highest number of migrating cells (634.70 ± 90.17), followed by PEC-NP-Exo group (444.30 ± 30.86), PEC-Exo group (318.30 ± 18.50), and PEC group (172.00 ± 76.08). Few migrating cells were observed in PCL group (16.00 ± 2.65) and blank group (6.67 ± 2.08) (Fig. 4A and C, enlarged images shown in Fig. S7).

Immunofluorescence staining, performed one week after the implantation of the membranes into the mouse cranial defect, showed a similar trend. A large number of BMSCs (SSEA4-positive, CD45-negative) were observed in PEC-Apt-NP-Exo group (35.40 ± 5.13). Moderate numbers of cells were found in PEC-NP-Exo group (19.20 ± 3.42) and PEC-Exo group (11.80 ± 2.95), with significantly more cells in PEC-NP-Exo group ($P < 0.01$). Small numbers of BMSCs were observed in PEC group (8.20 ± 1.30), and nearly no BMSCs were found in PCL group (1.40 ± 1.67) and blank group (2.20 ± 2.17) (Fig. 4B and D). These studies suggest that Apts, Exos, and PEC promote BMSC migration, and PEC-Apt-NP-Exo membrane, combining all three, effectively recruits BMSCs both *in vivo* and *in vitro*.

3.6. PEC-Apt-NP-Exos promoting macrophage polarization to M2

One week after membrane implantation *in vivo*, immunofluorescence staining was performed to identify M2 (CD68-positive, CD206-positive) and M1 (CD68-positive, CD80-positive) macrophages. The number of M2 macrophages in PEC-Apt-NP-Exo (76.60 ± 5.03) and PEC-NP-Exo (76.20 ± 2.86) groups was significantly higher than in PEC-Exo (51.60 ± 3.29) and PEC (50.60 ± 6.47) groups, whereas the number of M1 macrophages in PEC-Apt-NP-Exo (42.60 ± 5.81) and PEC-NP-Exo (45.20 ± 4.08) groups was significantly lower than in PEC-Exo (57.60 ± 7.30) and PEC (68.40 ± 9.10) groups. Notably, the numbers of M2 and M1 macrophages in PCL (M2: 4.40 ± 1.14; M1: 11.60 ± 2.70) and blank (M2: 2.80 ± 0.84; M1: 4.20 ± 2.86) groups were lower than those in the other groups due to the absence of tissue at the defect site. However, the M2/M1 ratio in PEC-Apt-NP-Exo (1.80 ± 0.12) and PEC-NP-Exo (1.69 ± 0.06) groups was significantly higher than in PEC-Exo (0.90 ± 0.06), PEC (0.74 ± 0.09), PCL (0.38 ± 0.10), and blank (0.67 ± 0.20) groups, with no significant difference between PEC-Apt-NP-Exo and PEC-NP-Exo groups (Fig. 5A–C). These results demonstrate that PEC-Apt-NP-Exo promotes macrophage polarization toward the M2 phenotype at the bone defect site through its Exo components.

3.7. PEC-Apt-NP-Exos promoting angiogenesis by Increasing the Secretion of VEGF in BMSCs

The interaction between BMSCs and endothelial cells is critical in vascularization during bone healing [41]. bEND.3 cells were cultured with BMSC supernatants (SN) treated using various methods, and angiogenic activity was then evaluated (Fig. 6A). As shown in Fig. 6B and D, both BMSC supernatants and Exos enhanced tube formation, and supernatants cultured with Exos further increased vascular junction formation. Similarly, BMSCs cultured with PEC-Apt-NP-Exo significantly enhanced tube formation in bEND.3 cells (Fig. 6C and E, enlarged images shown in Fig. S8.). VEGF serves as a key regulator of vascular development [42]. To further investigate the mechanism of vascularization, VEGF content was measured in the supernatants of BMSCs treated using various methods. VEGF secretion increased significantly from 90.40 ± 5.72 to 127.00 ± 16.50 ng/mL after BMSCs were cultured with Exos (Fig. 6F) and further increased to 173.6 ± 36.57 ng/mL following culture with PEC-Apt-NP-Exo membrane (Fig. 6G). These experiments demonstrate that PEC-Apt-NP-Exo membrane increases angiogenic activity *in vitro* by promoting VEGF secretion from BMSCs.

Immunohistochemical staining of CD31, conducted 4-week post-implantation, revealed that the number of new blood vessels in the PEC-Apt-NP-Exo (20.20 ± 2.59) and PEC-NP-Exo (19.80 ± 4.09) groups was significantly higher than in the PEC-Exo (13.60 ± 3.21), PEC (7.40 ± 3.21), PCL (9.40 ± 1.95), and blank (5.40 ± 2.41) groups (Fig. 6H and

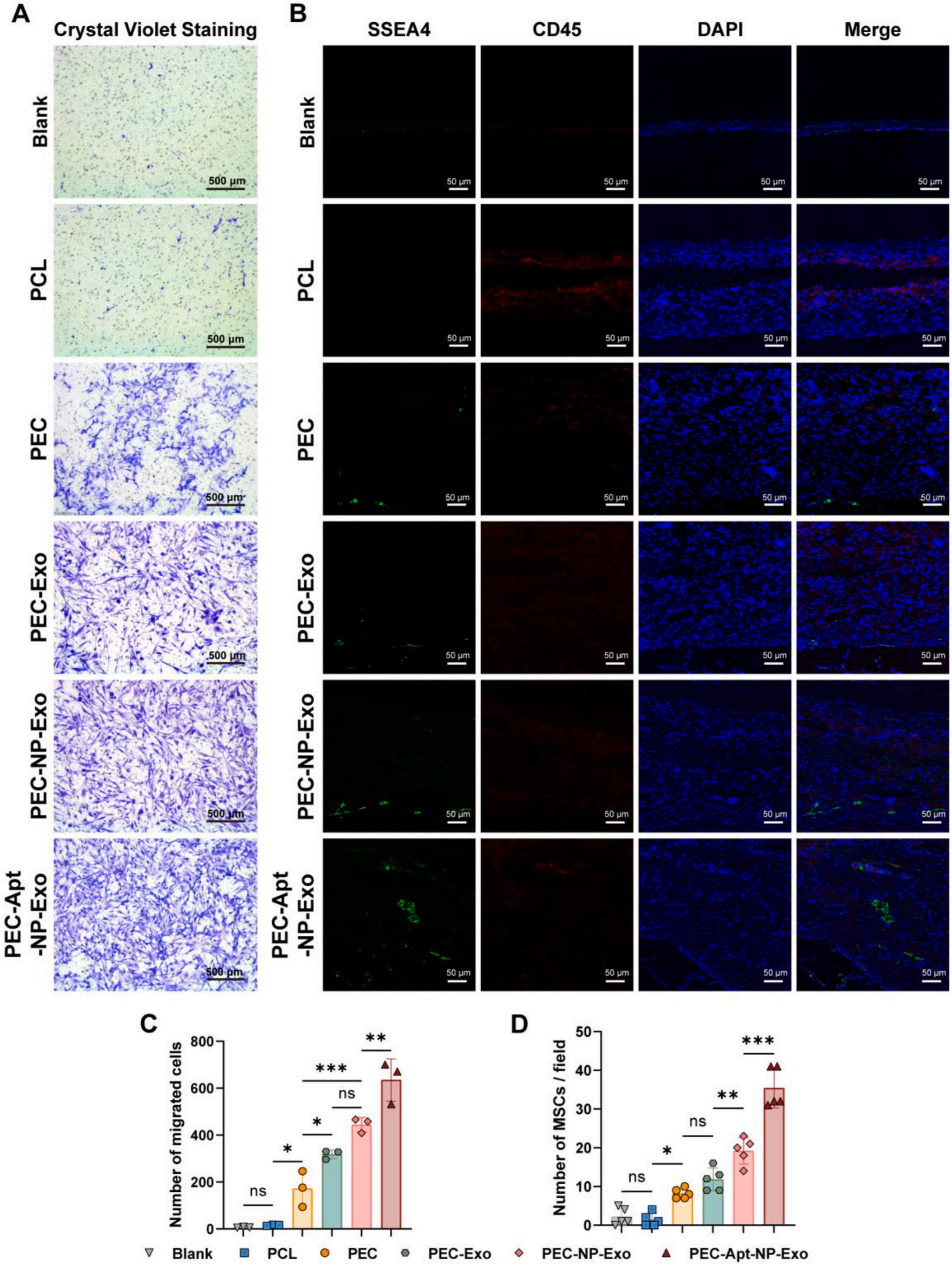

Fig. 4. PEC-Apt-NP-Exo promoting BMSC recruitment in the Early Stages of Bone Defects. (A) *In vitro* chemotactic behavior and (C) quantification of BMSCs on various membranes. (B) Representative images and (D) quantification of immunofluorescence staining one week after various membranes were implanted into critical-sized calvarial bone defects in mice. BMSCs were defined as SSEA4-positive and CD45-negative cells. Green: SSEA4; red: CD45; blue: DAPI-labeled cell nucleus. Data were shown as mean ± SDs. ns, no significance, ***$P < 0.001$, **$P < 0.01$, *$P < 0.05$.

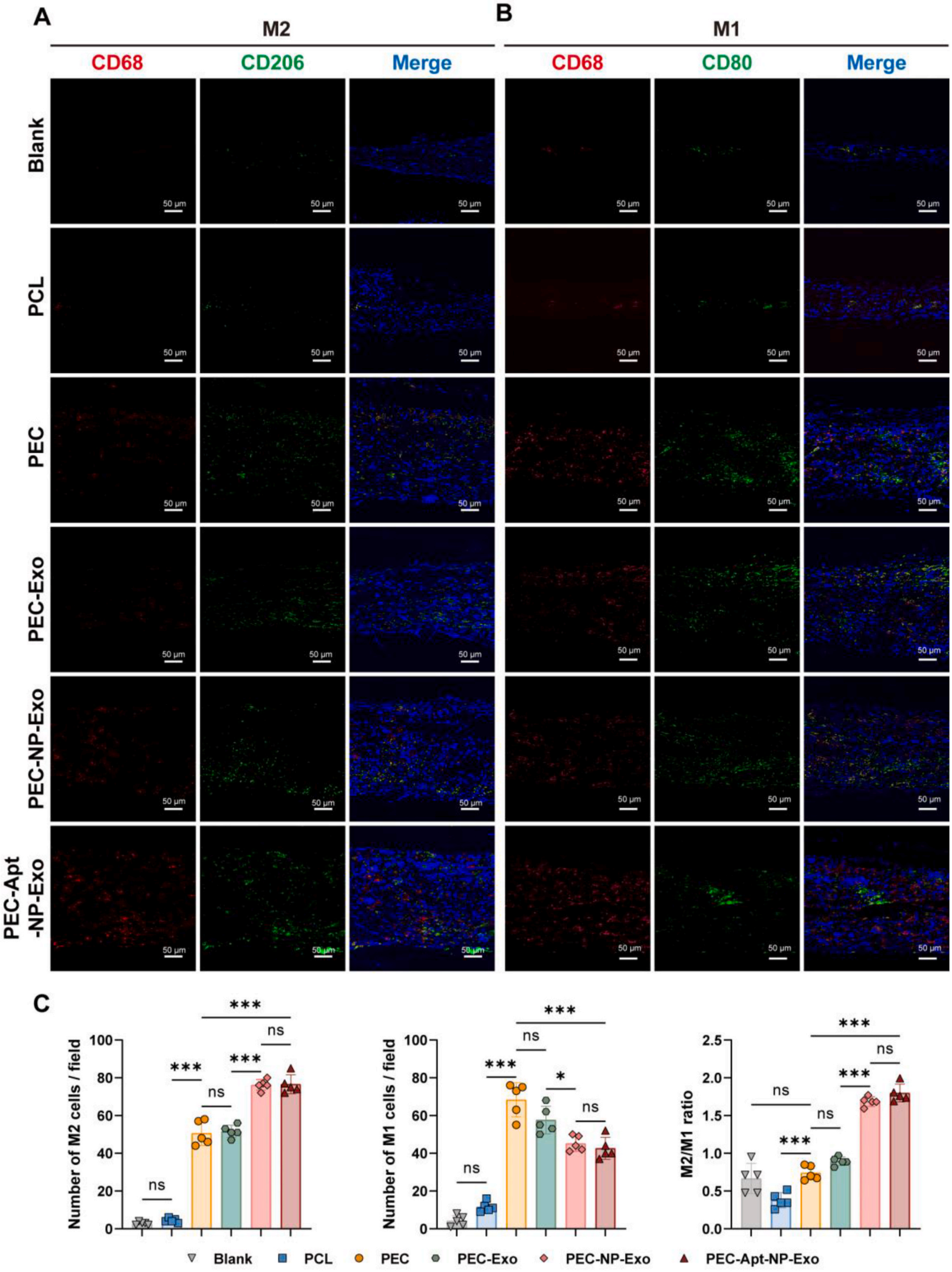

Fig. 5. PEC-Apt-NP-Exo Regulating the Early Immune Environment of Bone Defects. Immunofluorescence staining of (A) M2 macrophages (red: CD68; green: CD206; blue: nuclei) and (B) M1 macrophages (red: CD68; green: CD80; blue: nuclei) one week after the implantation of various membranes into critical-sized calvarial bone defects in mice. (C) Quantification of the number and ratio of M2 macrophages to M1 macrophages. Data were shown as mean ± SDs. ns, no significance, $***P < 0.001$, $**P < 0.01$, $*P < 0.05$.

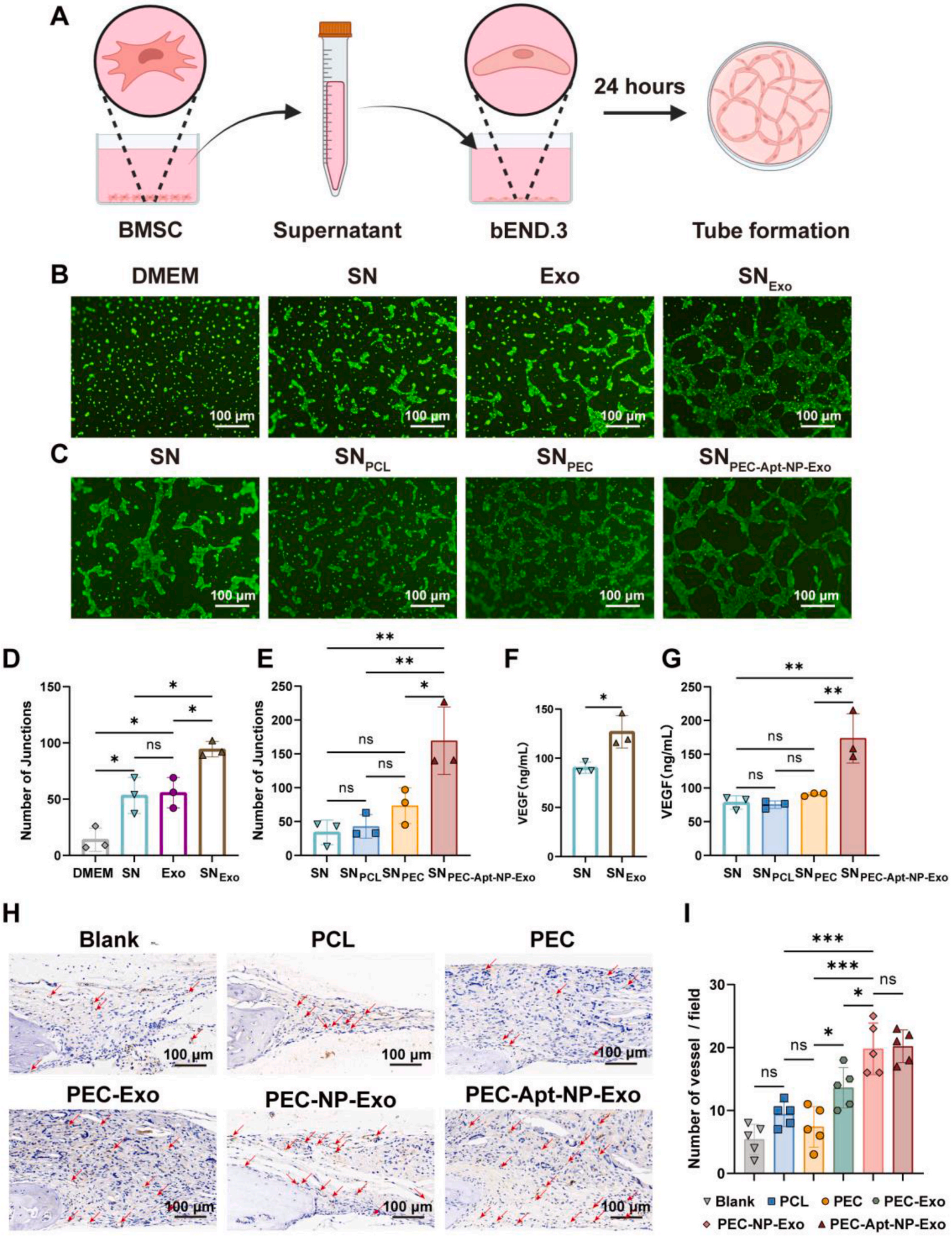

Fig. 6. Biomimetic Periosteum Promoting Angiogenesis by Increasing the Secretion of VEGF in BMSCs. (A) Schematic diagram of the experiment in which BMSCs regulate angiogenesis in bEND.3 cells. (B, C) Representative fluorescence images showing the promotion of tube formation after culturing BMSCs with (B) Exo or (C) various membranes, respectively. (D, E) Quantification of the number of junctions in the tube network. ELISA assay analyzes the VEGF content in the supernatant of BMSCs after co-culture with (F) Exos or (G) various membranes. (H) Representative images and (I) vascular quantification of CD31 immunohistochemical staining 4 weeks after various membranes was implanted into critical-sized calvarial bone defects in mice. Red arrows indicate blood vessels. Data were shown as mean ± SDs. ns, no significance, $^{***}P < 0.001$, $^{**}P < 0.01$, $^{*}P < 0.05$.

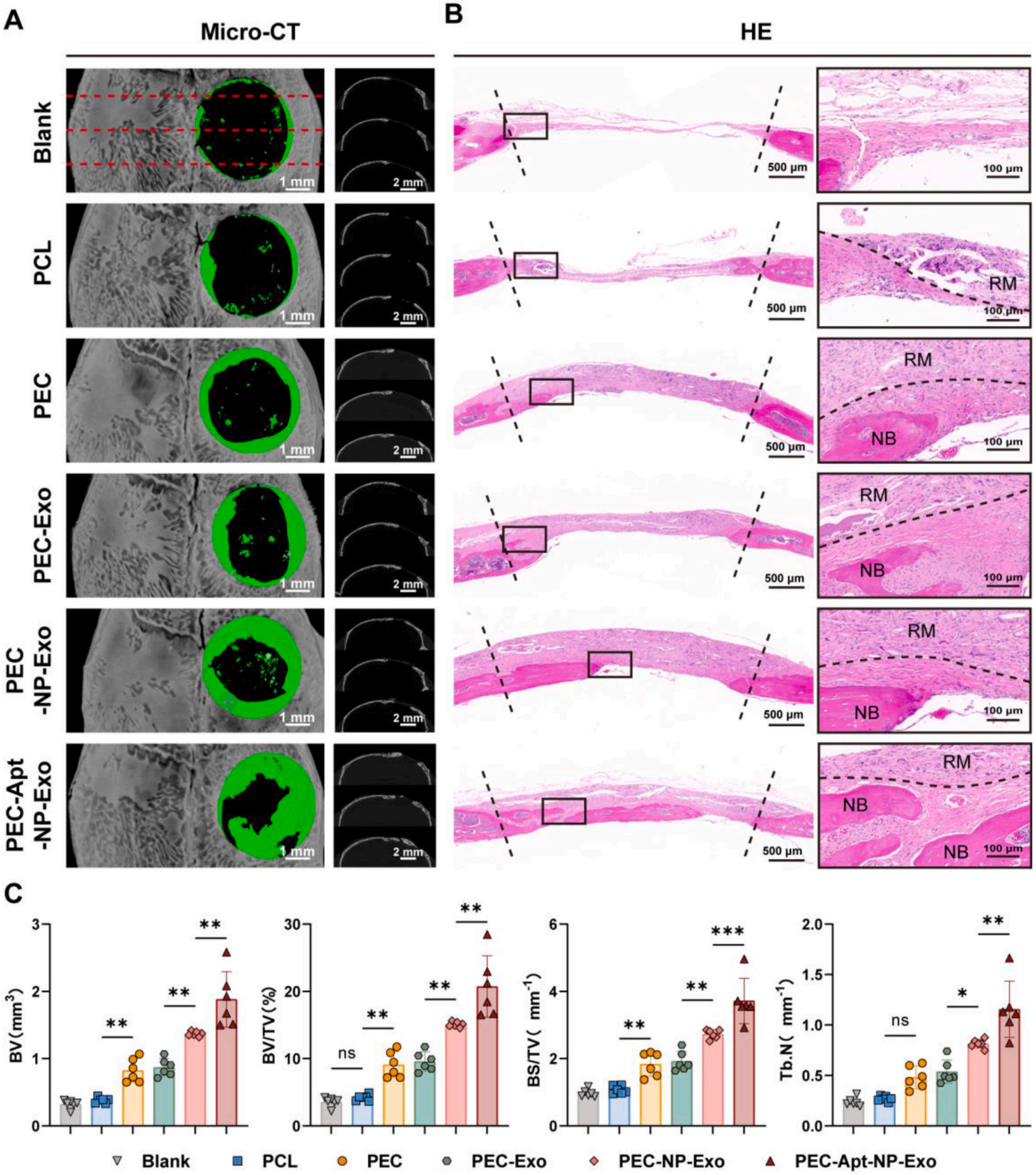

Fig. 7. PEC-Apt-NP-Exo Promoting the Regeneration of Critical-Sized Calvarial Bone Defects in Mice. Representative images of (A) micro-CT and (B) HE staining after 8-week implantation of various membranes on defects. RM: residual materials; NB: new bone; the dashed lines indicate the boundaries of the residual materials. (C) Quantitative analysis of osteogenesis-related parameters based on the 3D reconstruction micro-CT images. BV: bone volume; BV/TV: bone volume fraction; BS/TV: bone surface to tissue volume ratio; Tb.N: trabecular number. Data were shown as mean ± SDs. ns, no significance, $***P < 0.001$, $**P < 0.01$, $*P < 0.05$.

I). These results indicate that PEC-Apt-NP-Exo membrane promotes angiogenesis *in vivo*.

3.8. Bone regeneration with PEC-Apt-NP-Exos

Micro-CT scanning and reconstruction performed 8-week post-surgery revealed that the new bone volume (BV) in the PEC-Apt-NP-Exo group (1.88 ± 0.41 mm^3) was significantly greater than that in the PEC-NP-Exo group (1.37 ± 0.03 mm^3), which in turn was significantly greater than in the PEC-Exo group (0.87 ± 0.13 mm^3). The new bone volume in the PEC-Exo group, limited by the Exo loading capacity, was comparable to that in PEC group (0.82 ± 0.18 mm^3), but both were significantly higher than in PCL (0.38 ± 0.04 mm^3) and blank (0.32 ± 0.06 mm^3) groups. Bone volume/tissue volume (BV/TV), bone surface/tissue volume (BS/TV), and trabecular number (Tb.N) exhibited similar trends (Fig. 7A and C).

Histological analysis images revealed that only a small amount of fibrous tissue was present in the bone defect area without implanted materials, likely due to the absence of scaffolds for cell attachment in the control group. The PCL group maintained its intact and dense structure; however, due to the limited cell affinity of PCL, the material experienced minimal degradation and was encased by a thin layer of soft tissue. In contrast, the materials in the PEC, PEC-Exo, PEC-NP-Exo, and PEC-Apt-NP-Exo groups underwent extensive degradation, and the residual materials formed a multilayered structure. A large number of cells adhered to and proliferated on the loose residual materials, forming thicker new soft tissue, with new blood vessel formation observed, and new bone formation visible beneath the soft tissue (Fig. 7B).

3.9. PEC-Apt-NP-Exos regulating osteoblast differentiation to form new bone

OPN and OCN serve as key osteogenic markers [43]. Immunohistochemical staining revealed that the expression of OPN and OCN in PEC-Apt-NP-Exo group was significantly higher than in PEC and PCL groups ($P < 0.001$), with no significant difference compared to PEC-NP-Exo group. POSTN, a periosteum-specific marker, regulates osteoblast adhesion, migration, and differentiation, facilitating the secretion and mineralization of collagen matrix to form new bone [44,45]. POSTN expression in PEC-Apt-NP-Exo group was significantly higher than in the other groups ($P < 0.001$). Masson staining of bone collagen showed a larger bone matrix area in PEC-Apt-NP-Exo group compared to PEC-NP-Exo group ($P < 0.05$) and the other groups ($P < 0.001$) (Fig. 8A and B). These results suggest that PEC-Apt-NP-Exo regulates osteoblast differentiation and promotes new bone formation.

3.10. PEC-Apt-NP-Exos activating Rap1/PI3K/AKT signaling pathway

BMSCs were cultured on PEC-Apt-NP-Exo or PEC membranes for 7 days prior to transcriptome sequencing. Transcriptome analysis revealed 453 differentially expressed genes, with 281 upregulated and 172 downregulated in PEC-Apt-NP-Exo group compared to PEC group. KEGG enrichment analysis indicated activation of the Rap1 signaling pathway in PEC-Apt-NP-Exo group (Fig. 9A). GO enrichment analysis revealed that the differentially expressed genes were primarily associated with “regulation of cell migration”, “blood vessel morphogenesis”, and “extracellular matrix” functions (Fig. 9B). The volcano and heat maps illustrated the differentially expressed genes within the Rap1 signaling pathway. Notably, the expression of the pik3r1 gene, encoding PI3K within the Rap1 signaling pathway, was significantly increased (Fig. 9C and D). Previous studies have demonstrated that Rap1 participates in osteogenesis by activating the downstream PI3K/AKT signaling pathway [46]. To confirm this, the expression of key proteins involved in the Rap1/PI3K/AKT pathway was examined. Immunofluorescence staining revealed a significant enhancement of Rap1 expression in the PEC-Apt-NP-Exo group compared to the PEC group (Fig. S9). WB assay demonstrated significantly increased expression levels of Rap1, p-PI3K/PI3K, and p-AKT/AKT ratios in PEC-Apt-NP-Exo group (Fig. 9E and F). These findings indicate that the PEC-Apt-NP-Exo membrane activates the Rap1/PI3K/AKT signaling pathway in BMSCs, thereby upregulating the expression of downstream VEGF and RUNX2 to enhance angiogenesis and osteogenesis (Fig. 9G).

4. Discussion

The periosteum plays a crucial role throughout bone healing processes, including inflammatory responses, cellular recruitment, osteogenic differentiation, angiogenesis, bone matrix synthesis, and mineralization [47]. Therefore, artificial periostea have been designed to enhance regeneration in bone defects. Current artificial periostea are typically engineered to mimic the natural properties of periostea but struggle to replicate their multifaceted roles throughout the various stages of bone healing. Electrospun PCL membranes, recognized for their high mechanical properties and long-term stability, are commonly utilized for fabricating artificial periostea [48]. However, the synthetic polymer (such as PCL)-based artificial periostea are challenged with inflammation response triggered by biomaterials [49]. Moreover, PCL membranes lack bioactive properties and show limited effectiveness in repairing mouse calvarial defects (Fig. 7). ECM-based membranes, with good cell affinity and bioactive components, mitigate inflammation and reduce foreign body reactions; however, they lack stability and exhibit significant *in vitro* degradation after 7 days of incubation [15,50]. In this study, a biomimetic periosteum (termed PEC-Apt-NP-Exo) was fabricated using a PCL (core)-ECM (shell) coaxially electrospun membrane (PEC) and further modified with M2 macrophage-derived Apt NP-engineered exosomes (Apt-NP-Exo). The PEC, combining the mechanical properties of PCL and the bioactive properties of ECM, enabled the long-term coverage of bone defects and supported new bone formation (Fig. 7). Compared with PCL membranes, PEC significantly promotes *in vitro* cell proliferation and alleviates the *in vivo* pro-inflammatory environment in a cranial defect mouse model. To further emulate periosteum functions, Apt-NP-Exo were prepared and loaded onto the PEC.

M2 macrophage-derived exosomes play a crucial role in immunoregulation, angiogenesis, and osteogenesis during bone healing. However, the direct transplantation of Exos results in their rapid loss from targeted defect areas. In this study, M2 macrophage-derived Exos were modified with Apt-NPs, which contained three functional groups: cholesterol (bonding Exos), Apt (targeting BMSCs), and AF647 (fluorescent labeling). This modification did not negatively affect the bioactivity of Exos. The size, morphology, and marker protein expression of Apt-NP-Exo were similar to those of Exos (Fig. 1). Furthermore, the amino groups on the Apt of Apt-NP-Exo were covalently linked to the carboxyl groups on the ECM surface of PEC through EDC/NHS chemistry, forming Apt-NP-Exo-coated PEC and enabling the recruitment of endogenous BMSCs and the long-term release of Exos in bone defects. Both the 24-h Transwell assay *in vitro* and the 7-day immunofluorescence assay *in vivo* confirmed that the number of BMSCs migrating to the PEC-Apt-NP-Exo group was significantly higher than in other groups (Fig. 4). Notably, the PEC-Apt-NP-Exo group recruited more BMSCs than the PEC-NP-Exo group, demonstrating that Apt-based modifications enhance Exo utilization by target cells. Moreover, the PEC-Apt-NP-Exo sustainably released Apt-NP-Exo in 8 days (Fig. 3) and promoted M2 macrophage polarization, endogenous BMSC recruitment, osteogenic differentiation, vascularization, and new bone formation. These findings confirm that the PEC-Apt-NP-Exo membrane effectively recruits and differentiates BMSCs into osteoblasts in both *in vitro* and *in vivo* settings.

M2 macrophage-derived Exos can regulate the initial inflammatory phase of bone healing. Periosteal inflammatory reactions occur in the early stages of bone defects (24–48 h) [51]. Inflammatory conditions drive BMSCs toward adipogenic rather than osteogenic differentiation [52]. An immune microenvironment dominated by M1 macrophages

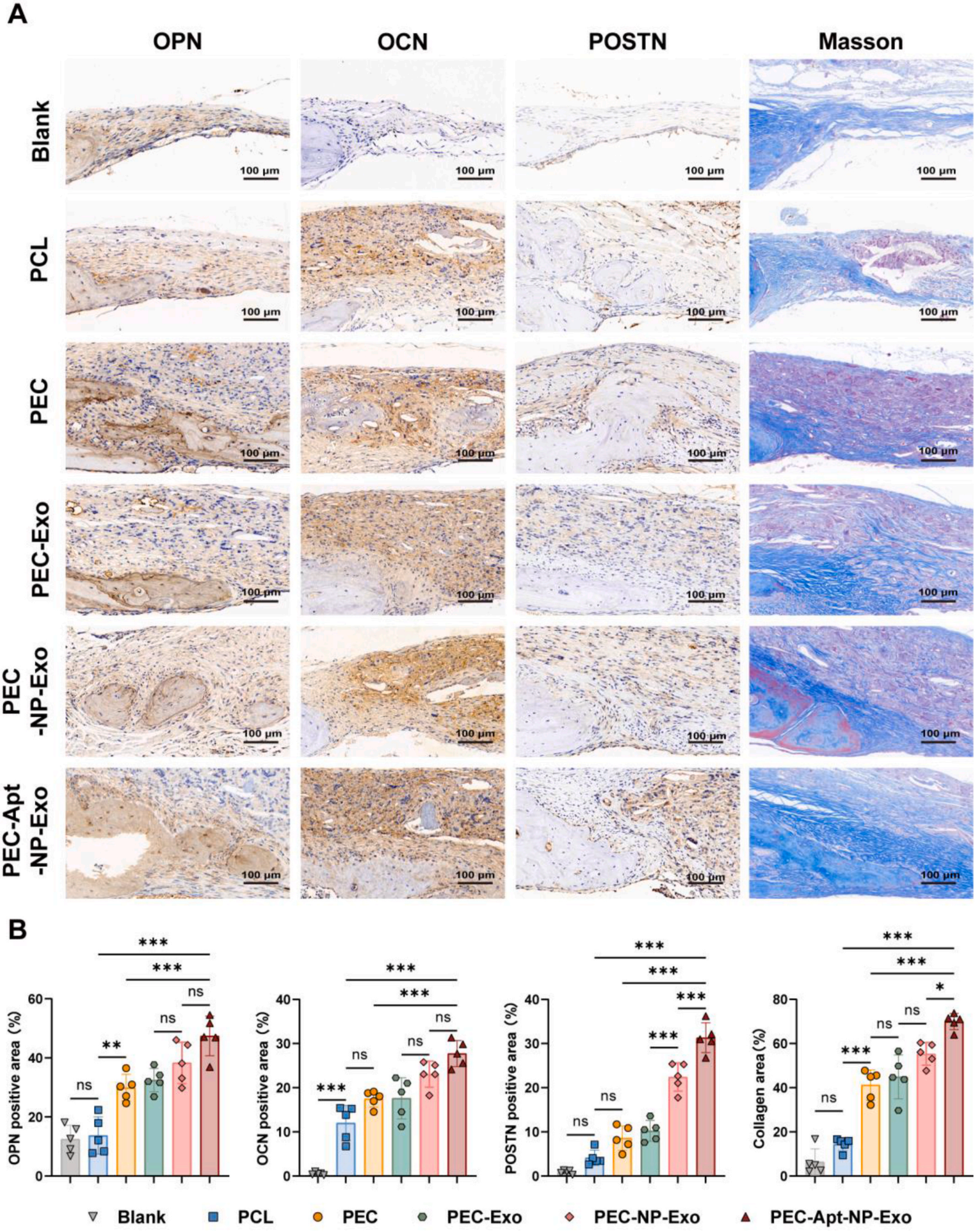

Fig. 8. PEC-Apt-NP-Exo Promoting New Bone Formation by Enhancing Osteoblast Differentiation in the Late Stage of Bone Defects. (A) Histological staining and (B) quantification of OPN, OCN, POSTN, and Masson after 8 weeks of implantation of various membranes on defects. Data were shown as mean ± SDs. ns, no significance, ***$P < 0.001$, **$P < 0.01$, *$P < 0.05$.

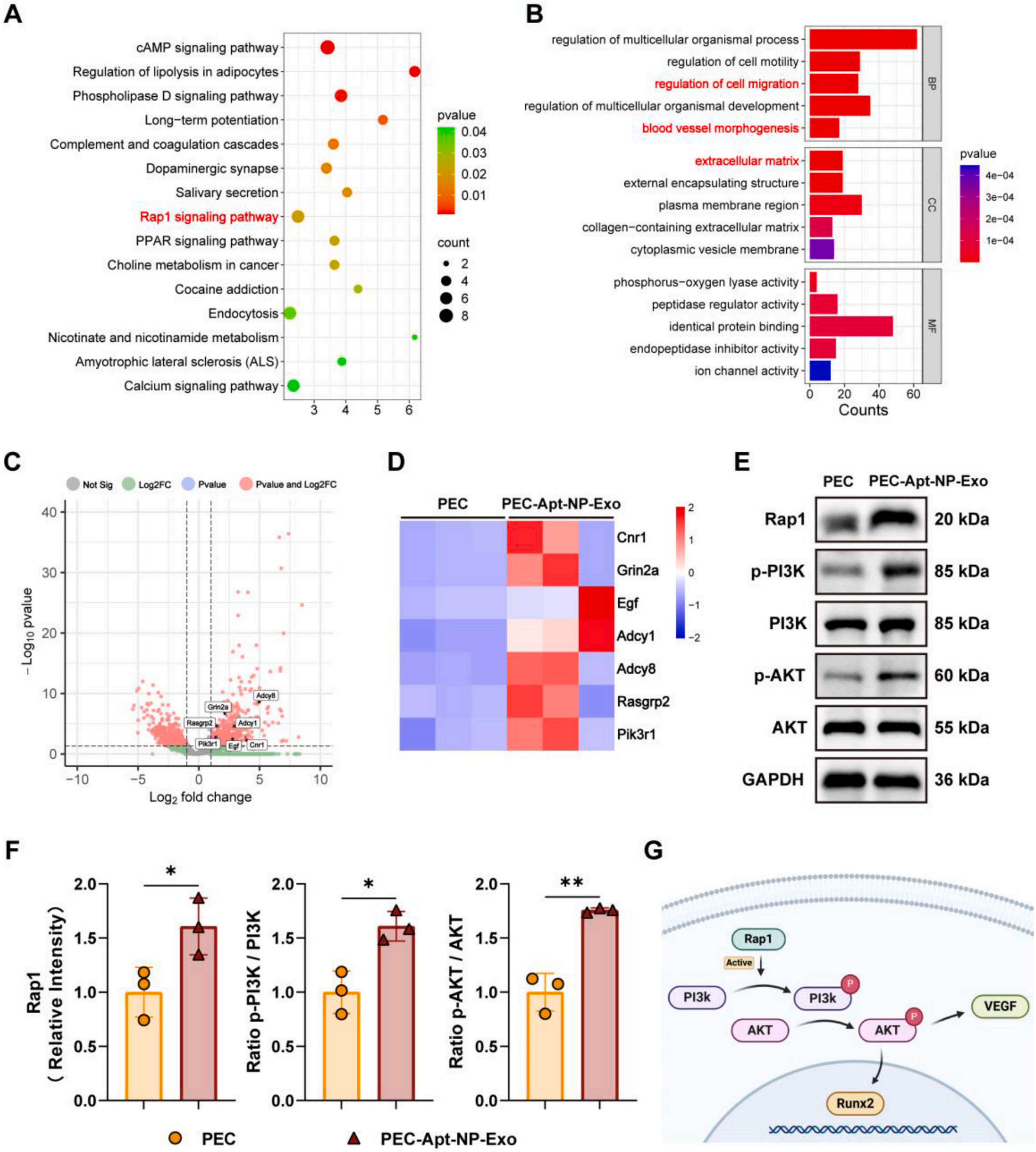

Fig. 9. PEC-Apt-NP-Exo Promoting Vascularization and Osteogenesis via the Rap1/PI3K/AKT Signaling Axis. (A) KEGG enrichment analysis following the sequencing of BMSCs cultured with PEC or PEC-Apt-NP-Exo. (B) GO enrichment analysis. BP: biological process, CC: cellular component, MF: molecular function. (C) Volcano plot showing the distribution of genes related to the Rap1 signaling pathway. (D) Heatmap of significantly differentially expressed genes in the Rap1 signaling pathway. (E) Protein expression levels of Rap1, p-PI3K, PI3K, p-AKT, and AKT were detected by WB in BMSCs. (F) Quantitative expression levels of Rap1, p-PI3K, PI3K, p-AKT, and AKT. (G) Schematic diagram illustrating the action mechanism of the PEC-Apt-NP-Exo membrane. Data were shown as mean ± SDs. ns, no significance, ***$P < 0.001$, **$P < 0.01$, *$P < 0.05$.

activates osteoclast activity and promotes the production of pro-inflammatory factors, which hinders bone repair [53]. Increasing the proportion of M2 macrophages enhances osteoblast activity and subsequently promotes bone formation [54]. Therefore, reducing M1 macrophages while increasing M2 macrophages has been a longstanding therapeutic goal in bone regeneration [55]. M2 macrophages regulate bone regeneration primarily through their Exos. Recent studies have demonstrated that the M2 macrophage-derived Exos induce M1 macrophages to differentiate into M2 macrophages by activating the PI3K/AKT pathway [56]. Exos circumvent immune rejection associated with cells and are considered gentler, safer, and more natural than the direct implantation of cells or cytokines. In this study, we implanted M2 macrophage-derived Exos-anchored PEC-Apt-NP-Exo in a cranial defect model, for reducing Exo consumption by the circulatory system and enhancing Exo aggregation at the bone defect site. Furthermore, we observed that the differentiation effect of M2 macrophages improved with increased Exos loading. Through covalently bonding Exos, PEC-Apt-NP-Exo and PEC-NP-Exo groups significantly reduced M1 macrophage numbers and enhanced M2 macrophage polarization compared to PEC-Exo. The efficient loading of Exos facilitated the creation of an immune microenvironment dominated by M2 macrophages during the early stages of bone healing, thereby establishing favorable conditions for subsequent bone formation.

Following the inflammation regulation, recruitment and differentiation of endogenous BMSC are important in bone healing. Previous artificial periosteum designs relied on the delivery of exogenous BMSCs; however, this approach faces challenges, including low cell survival and the potential for immune rejection [57,58]. Several biomolecules have been explored for their ability to recruit endogenous BMSCs, including interleukin-6, interleukin-8, VEGF, BMP-2, and SDF-1 [59–63]. However, cytokines lack target specificity and may produce adverse effects. In contrast to functional proteins, Apts exhibit greater specificity and affinity for their targets [64–66]. In this study, we prepared Apt-anchored Exos (Apt-NP-Exo) and bound them on PEC for promoting recruitment and differentiation of endogenous BMSC simultaneously. The Apt was anchored to the lipid bilayer membrane of the Exos via cholesterol insertion. Insertion of lipophilic molecules, such as cholesterol or phospholipids, is a widely employed method for Exo surface modification. In this study, cholesterol serves as a medium to link Exo to Apt-NP, as its lower incubation temperature compared to phospholipids helps preserve the active components of Exo and maintain their stability [67]. Apt-NP-Exo exhibited greater aggregation in BMSCs compared to Exo, proving that the surface-attached Apt enhanced the affinity of Exos for BMSCs. This increased affinity facilitates the internalization of Exos by BMSCs within the complex bone repair environment.

Vascularization is a well-established prerequisite for effective bone regeneration [68]. After bone injury, an adequate blood supply from the periosteum ensures the smooth progression of osteogenesis. *In vitro* pre-vascularization utilizing endothelial cell/BMSC co-culture systems is a primary method for inducing vascularization [69]. However, the co-culture systems exhibit significant limitations in forming stable vascular networks and fusing with host blood vessels [70]. Previous studies demonstrated that both M2 macrophages and BMSCs can secrete VEGF and facilitate the vascularized process [71,72]. These findings suggest that enhancing crosstalk between endothelial cells and macrophages or BMSCs could improve endogenous angiogenesis and osteogenesis. In this study, BMSCs cultured with M2 macrophage-derived Exos enhanced vascular tubule formation, indicating that the Exos enhance the regulatory effect of BMSCs on endothelial cells and promote angiogenesis. ELISA results proved that the enhanced regulation was mediated by the Exo-induced VEGF secretion of BMSCs increasing. In a cranial defect model, PEC-Apt-NP-Exo and PEC-NP-Exo groups exhibited significantly greater vascular formation after 4 weeks of implantation than other groups. The ability to promote angiogenesis would support subsequent osteogenesis in bone repair.

The efficacy of PEC-Apt-NP-Exo on osteogenic regeneration was evaluated by animal experiments. Immunohistochemical staining revealed that the classic osteogenic markers OPN and OCN were enriched in PEC-Apt-NP-Exo group at 8 weeks post-implantation. Meanwhile, the expression of POSTN, a periosteum-specific marker, was highest in PEC-Apt-NP-Exo group. POSTN is recognized as a key regulator in maintaining the periosteal cell pool, playing a crucial role in osteoblast differentiation and accelerating mesenchymal stem cell-mediated osteogenesis [73,74]. Osteoblasts are the primary functional cells responsible for bone formation, including the secretion and mineralization of the bone matrix. Masson staining results showed that blue-stained bone matrix in PEC-Apt-NP-Exo group gradually migrated toward the red-stained membrane, and the content of the bone matrix was significantly higher than that in other groups. Micro-CT was subsequently employed to assess bone matrix mineralization. The PEC-Apt-NP-Exo group exhibited the highest level of new bone formation, followed by the PEC-NP-Exo group. This indicates that the covalent binding of Apt-NP-Exo or NP-Exo on the PEC significantly increases Exo loading and new bone formation, and Apt modification further improves Exo targeting to BMSC and BMSC recruiting. These results demonstrate that PEC-Apt-NP-Exo membrane regulates osteoblast differentiation, promoting bone matrix formation and mineralization, ultimately enhancing osteogenesis.

Mechanistically, previous studies have reported that M2 macrophages promote osteogenic differentiation of BMSCs through the PI3K/AKT signaling pathway [56,75]. In this study, PEC-Apt-NP-Exo membrane was found to activate both the Rap1 and PI3K/AKT signaling pathways (Fig. 9). Rap1, a member of the Ras superfamily of small GTPases, is regulated by Rap1 GTPase-activating protein and Rap1-specific guanine nucleotide exchange factor and can activate downstream ERK and PI3K/AKT signaling pathways [76–78]. Thus, we propose that PEC-Apt-NP-Exo membrane promotes osteogenesis via the Rap1/PI3K/AKT signaling axis. The PI3K/AKT signaling pathway is a well-established regulator of cell metabolism and is involved in processes such as cell migration, angiogenesis, bone growth, and macrophage polarization [79,80]. The PI3K/AKT signaling pathway stimulates RUNX2 expression and activity through direct or indirect mechanisms, contributing to the regulation of osteogenic differentiation [81,82]. Additionally, VEGF expression is positively correlated with the PI3K/AKT signaling pathway, and the two synergistically promote angiogenesis [83,84]. We demonstrated that PEC-Apt-NP-Exo increased the expression of Runx2 and VEGF in BMSCs. Taken together, these findings demonstrate that the PEC-Apt-NP-Exo membrane induces cell chemotaxis and migration through the Rap1/PI3K/AKT signaling pathway, thereby facilitating the recruitment of BMSCs to the defect site. This process upregulates the expression of downstream Runx2 and VEGF by activating AKT kinase. The increased expression of Runx2 promotes the osteogenic differentiation of BMSCs, while VEGF enhances angiogenesis in endothelial cells, supporting the regeneration of the vascular network at the bone defect site and ultimately accelerating osteogenesis.

Similar to other physiological processes in the human body, the regulation of bone regeneration by the periosteum is a complex and highly coordinated mechanism. Simulating the individual functions of the periosteum is insufficient to address the comprehensive needs of bone regeneration. Drawing upon the mechanisms by which the periosteum regulates bone regeneration, we developed a multifunctional biomimetic periosteum (i.e., PEC-Apt-NP-Exo) capable of simulating the periosteum regulation of inflammation, stem cell recruitment and differentiation, angiogenesis, bone matrix synthesis, and mineralization after bone defects. However, despite its promise as a biomaterial for addressing clinical challenges, more research is necessary to improve the stability and efficiency of engineered Exos. In this study, the low insertion stability of cholesterol anchor molecules resulted in suboptimal assembly efficiency of engineered Exo. Future research may achieve improved results by adopting chemical strategies such as thiol-maleimide coupling, azide-alkyne cycloaddition, or amidation chemistry to modify the Exo surface [85]. In addition, this study establishes a novel system for the local enrichment and controlled release of engineered exosomes, specifically targeting certain cells to achieve sustained delivery for long-term bioactive effects. This approach provides a distinctive method for the targeted delivery of regenerative signals. Future research may broaden the application of biomimetic periosteum by incorporating drug-loaded exosomes to facilitate the localized, sustained release of therapeutic agents and evaluate its potential to repair larger bone defects in large animal models. Such developments could lead to more effective and targeted treatments for bone defects while offering clearer clinical perspectives. The Apt used in this study was designed for high-affinity binding to BMSCs. These aptamers were validated in previous research and the current study for their specificity and minimal binding to non-target cells. However, due to the natural affinity of the Exo envelope for the cell membrane, the Apt cannot completely prevent the inherent binding of the Exo to other cells, making off-target effects of the Exo unavoidable. Future studies may explore alternative carriers to minimize potential off-target effects.

5. Conclusion

Drawing inspiration from the bone healing process and the multifunctionality of the periosteum, we successfully developed a multifunctional biomimetic periosteum featuring an electrospun PCL core-ECM shell fiber membrane combined with M2 macrophage-derived engineered Exos. *In vitro* studies reveal that the biomimetic periosteum significantly upregulates the Rap1/PI3K/AKT signaling pathway and VEGF secretion of BMSCs through the specific targeting of the engineered Exos. These suggest that the biomimetic periosteum possesses pro-osteogenic and angiogenic capability. Moreover, animal model studies demonstrate the biomimetic periosteum modulates M2 macrophage polarization, recruits endogenous BMSCs, and induces osteogenic differentiation during the early stages of bone defects, ultimately promotes vascularization and ossification of callus tissue. This research offers insights into the future design of multifunctional biomimetic periosteum constructs for bone defect repair.

Ethics approval and consent to participate

All procedures were conducted in accordance with the Guidelines for the Care and Use of Laboratory Animals of the Guangdong Academy of Medical Sciences and approved by the Ethics Committee for Animal Experiments (No. KY2023-584-01).

CRediT authorship contribution statement

Zhuohao Wen: Writing – original draft, Visualization, Validation, Methodology, Investigation, Formal analysis, Data curation, Conceptualization. **Shuyi Li:** Writing – review & editing, Supervision, Methodology, Conceptualization. **Yi Liu:** Writing – review & editing, Visualization, Methodology. **Xueyan Liu:** Validation, Investigation, Formal analysis. **Huiguo Qiu:** Investigation. **Yuejuan Che:** Writing – review & editing, Supervision. **Liming Bian:** Writing – review & editing, Supervision. **Miao Zhou:** Supervision, Project administration, Funding acquisition.

Declaration of competing interest

The authors declare no conflict of interest.

Acknowledgements

This work was supported by the National Natural Science Foundation of China (Grant No. 82301025), the Talents Introduction of Guangdong Provincial People's Hospital (Grant Nos. KY0120220255, 3227100558, and 8237030185), Guangzhou Municipal Science and Technology Bureau (Grant No. 2024A04J4888), the National Key Research and Development Program of China (Grant No. 2023YFC2413600), the Natural Science Foundation of Guangdong Province (Grant No. 2022A1515110916). This work was also supported by the GJYC program of Guangzhou (Grant No. 2024D03J0004) and the National Natural Science Foundation of China (Grant No. 52433010).

Appendix A. Supplementary data

Supplementary data to this article can be found online at https://doi.org/10.1016/j.bioactmat.2025.03.027.

References

[1] M.R. Allen, J.M. Hock, D.B. Burr, Periosteum: biology, regulation, and response to osteoporosis therapies, Bone 35 (5) (2004) 1003–1012.
[2] Z. Lin, A. Fateh, D.M. Salem, G. Intini, Periosteum: biology and applications in craniofacial bone regeneration, J. Dent. Res. 93 (2) (2014) 109–116.
[3] C. Colnot, Skeletal cell fate decisions within periosteum and bone marrow during bone regeneration, J. Bone Miner. Res. 24 (2) (2009) 274–282.
[4] X. Zhang, C. Xie, A.S. Lin, H. Ito, H. Awad, J.R. Lieberman, P.T. Rubery, E. M. Schwarz, R.J. O'Keefe, R.E. Guldberg, Periosteal progenitor cell fate in segmental cortical bone graft transplantations: implications for functional tissue engineering, J. Bone Miner. Res. 20 (12) (2005) 2124–2137.
[5] F. Loi, L.A. Cordova, J. Pajarinen, T.H. Lin, Z. Yao, S.B. Goodman, Inflammation, fracture and bone repair, Bone 86 (2016) 119–130.
[6] M.N. Michalski, L.K. McCauley, Macrophages and skeletal health, Pharmacol. Ther. 174 (2017) 43–54.
[7] C.S. Bahney, R.L. Zondervan, P. Allison, A. Theologis, J.W. Ashley, J. Ahn, T. Miclau, R.S. Marcucio, K.D. Hankenson, Cellular biology of fracture healing, J. Orthop. Res. 37 (1) (2019) 35–50.
[8] G. Zhu, T. Zhang, M. Chen, K. Yao, X. Huang, B. Zhang, Y. Li, J. Liu, Y. Wang, Z. Zhao, Bone physiological microenvironment and healing mechanism: basis for future bone-tissue engineering scaffolds, Bioact. Mater. 6 (11) (2021) 4110–4140.
[9] X. Wang, Y. Liang, J. Li, J. Wang, G. Yin, Z. Chen, Z. Huang, X. Pu, Artificial periosteum promotes bone regeneration through synergistic immune regulation of aligned fibers and BMSC-recruiting phages, Acta Biomater. 180 (2024) 262–278.
[10] W. Zhang, T. Sun, J. Zhang, X. Hu, M. Yang, L. Han, G. Xu, Y. Zhao, Z. Li, Construction of artificial periosteum with methacrylamide gelatin hydrogel-wharton's jelly based on stem cell recruitment and its application in bone tissue engineering, Mater. Today. Bio 18 (2023) 100528.
[11] B.G. Matthews, S. Novak, F.V. Sbrana, J.L. Funnell, Y. Cao, E.J. Buckels, D. Grcevic, I. Kalajzic, Heterogeneity of murine periosteum progenitors involved in fracture healing, Elife 10 (2021).
[12] L. Li, J. Li, J. Guo, H. Zhang, X. Zhang, C. Yin, L. Wang, Y. Zhu, Q. Yao, 3D molecularly functionalized cell-free biomimetic scaffolds for osteochondral regeneration, Adv. Funct. Mater. 29 (6) (2018).
[13] X. Xue, H. Zhang, H. Liu, S. Wang, J. Li, Q. Zhou, X. Chen, X. Ren, Y. Jing, Y. Deng, Z. Geng, X. Wang, J. Su, Rational design of multifunctional CuS nanoparticle-PEG composite soft hydrogel-coated 3D hard polycaprolactone scaffolds for efficient bone regeneration, Adv. Funct. Mater. 32 (33) (2022).
[14] X. Lin, C. Zhao, P. Zhu, J. Chen, H. Yu, Y. Cai, Q. Zhang, A. Qin, S. Fan, Periosteum extracellular-matrix-mediated acellular mineralization during Bone Formation, Adv. Healthcare Mater. 7 (4) (2018).
[15] S. Li, R. Deng, T. Forouzanfar, G. Wu, D. Quan, M. Zhou, Decellularized periosteum-derived hydrogels promote the proliferation, migration and osteogenic differentiation of human umbilical cord mesenchymal stem cells, Gels 8 (5) (2022).
[16] S. Li, R. Deng, X. Zou, Q. Rong, J. Shou, Z. Rao, W. Wu, G. Wu, D. Quan, M. Zhou, T. Forouzanfar, Development and fabrication of co-axially electrospun biomimetic periosteum with a decellularized periosteal ECM shell/PCL core structure to promote the repair of critical-sized bone defects, Compos. B Eng. 234 (2022).
[17] J. Ping, C. Zhou, Y. Dong, X. Wu, X. Huang, B. Sun, B. Zeng, F. Xu, W. Liang, Modulating immune microenvironment during bone repair using biomaterials: Focusing on the role of macrophages, Mol. Immunol. 138 (2021) 110–120.
[18] Y. Zhang, T. Bose, R.E. Unger, J.A. Jansen, C.J. Kirkpatrick, J. van den Beucken, Macrophage type modulates osteogenic differentiation of adipose tissue MSCs, Cell Tissue Res. 369 (2) (2017) 273–286.
[19] L. Gong, Y. Zhao, Y. Zhang, Z. Ruan, The macrophage polarization regulates MSC osteoblast differentiation in vitro, Ann. Clin. Lab. Sci. 46 (1) (2016) 65–71.
[20] M. Kang, C.C. Huang, Y. Lu, S. Shirazi, P. Gajendrareddy, S. Ravindran, L. F. Cooper, Bone regeneration is mediated by macrophage extracellular vesicles, Bone 141 (2020) 115627.
[21] X. Chen, Z. Wan, L. Yang, S. Song, Z. Fu, K. Tang, L. Chen, Y. Song, Exosomes derived from reparative M2-like macrophages prevent bone loss in murine periodontitis models via IL-10 mRNA, J Nanobiotechnology 20 (1) (2022) 110.
[22] S. Jin, J. Wen, Y. Zhang, P. Mou, Z. Luo, Y. Cai, A. Chen, X. Fu, W. Meng, Z. Zhou, J. Li, W. Zeng, M2 macrophage-derived exosome-functionalized topological scaffolds regulate the foreign body response and the coupling of angio/osteoclasto/osteogenesis, Acta Biomater. 177 (2024) 91–106.
[23] C.P. Lai, O. Mardini, M. Ericsson, S. Prabhakar, C. Maguire, J.W. Chen, B. A. Tannous, X.O. Breakefield, Dynamic biodistribution of extracellular vesicles in vivo using a multimodal imaging reporter, ACS Nano 8 (1) (2014) 483–494.

[24] W. Meng, C. He, Y. Hao, L. Wang, L. Li, G. Zhu, Prospects and challenges of extracellular vesicle-based drug delivery system: considering cell source, Drug Deliv. 27 (1) (2020) 585–598.

[25] H. Wang, Y. Guo, Y. Jiang, Y. Ge, H. Wang, D. Shi, G. Zhang, J. Zhao, Y. Kang, L. Wang, Exosome-loaded biomaterials for tendon/ligament repair, Biomater Transl 5 (2) (2024) 129–143.

[26] L. Wu, Y. Wang, X. Xu, Y. Liu, B. Lin, M. Zhang, J. Zhang, S. Wan, C. Yang, W. Tan, Aptamer-based detection of circulating targets for Precision medicine, Chem Rev 121 (19) (2021) 12035–12105.

[27] N.F. Hosseini, R. Amini, M. Ramezani, M. Saidijam, S.M. Hashemi, R. Najafi, AS1411 aptamer-functionalized exosomes in the targeted delivery of doxorubicin in fighting colorectal cancer, Biomed. Pharmacother. 155 (2022) 113690.

[28] Y. Su, Q. Gao, R. Deng, L. Zeng, J. Guo, B. Ye, J. Yu, X. Guo, Aptamer engineering exosomes loaded on biomimetic periosteum to promote angiogenesis and bone regeneration by targeting injured nerves via JNK3 MAPK pathway, Mater Today Bio 16 (2022) 100434.

[29] D. Shu, Y. Shu, F. Haque, S. Abdelmawla, P. Guo, Thermodynamically stable RNA three-way junction for constructing multifunctional nanoparticles for delivery of therapeutics, Nat. Nanotechnol. 6 (10) (2011) 658–667.

[30] S. Guo, X. Piao, H. Li, P. Guo, Methods for construction and characterization of simple or special multifunctional RNA nanoparticles based on the 3WJ of phi29 DNA packaging motor, Methods 143 (2018) 121–133.

[31] L. Guo, D. Shi, M. Shang, X. Sun, D. Meng, X. Liu, X. Zhou, J. Li, Utilizing RNA nanotechnology to construct negatively charged and ultrasound-responsive nanodroplets for targeted delivery of siRNA, Drug Deliv. 29 (1) (2022) 316–327.

[32] J. Moon, J. Lim, S. Lee, H.Y. Son, H.W. Rho, H. Kim, H. Kang, J. Jeong, E.K. Lim, J. Jung, Y.M. Huh, H.G. Park, T. Kang, Urinary exosomal mRNA detection using novel isothermal gene amplification method based on three-way junction, Biosens. Bioelectron. 167 (2020) 112474.

[33] J. Bai, Y. Luo, X. Wang, S. Li, M. Luo, M. Yin, Y. Zuo, G. Li, J. Yao, H. Yang, M. Zhang, W. Wei, M. Wang, R. Wang, C. Fan, Y. Zhao, A protein-independent fluorescent RNA aptamer reporter system for plant genetic engineering, Nat. Commun. 11 (1) (2020) 3847.

[34] D. Xiao, Y. Huang, S. Huang, J. Zhuang, P. Chen, Y. Wang, L. Zhang, Targeted delivery of cancer drug paclitaxel to chordomas tumor cells via an RNA nanoparticle harboring an EGFR aptamer, Colloids Surf. B Biointerfaces 212 (2022) 112366.

[35] C.J. Li, P. Cheng, M.K. Liang, Y.S. Chen, Q. Lu, J.Y. Wang, Z.Y. Xia, H.D. Zhou, X. Cao, H. Xie, E.Y. Liao, X.H. Luo, MicroRNA-188 regulates age-related switch between osteoblast and adipocyte differentiation, J. Clin. Investig. 125 (4) (2015) 1509–1522.

[36] Z.W. Luo, F.X. Li, Y.W. Liu, S.S. Rao, H. Yin, J. Huang, C.Y. Chen, Y. Hu, Y. Zhang, Y.J. Tan, L.Q. Yuan, T.H. Chen, H.M. Liu, J. Cao, Z.Z. Liu, Z.X. Wang, H. Xie, Aptamer-functionalized exosomes from bone marrow stromal cells target bone to promote bone regeneration, Nanoscale 11 (43) (2019) 20884–20892.

[37] J. Shou, S. Li, W. Shi, S. Zhang, Z. Zeng, Z. Guo, Z. Ye, Z. Wen, H. Qiu, J. Wang, M. Zhou, 3WJ RNA nanoparticles-aptamer functionalized exosomes from M2 macrophages target BMSCs to promote the healing of bone fractures, Stem Cells Transl Med 12 (11) (2023) 758–774.

[38] M. Piao, S.H. Lee, M.J. Kim, J.K. Choi, C.Y. Yeo, K.Y. Lee, Cyclophilin A promotes osteoblast differentiation by regulating Runx2, Int. J. Mol. Sci. 23 (16) (2022).

[39] L. Oliver-Cervello, H. Martin-Gomez, N. Mandakhbayar, Y.W. Jo, E.A. Cavalcanti-Adam, H.W. Kim, M.P. Ginebra, J.H. Lee, C. Mas-Moruno, Mimicking bone extracellular matrix: from BMP-2-derived sequences to osteogenic-multifunctional coatings, Adv. Healthcare Mater. 11 (20) (2022) e2201339.

[40] J. Si, C. Wang, D. Zhang, B. Wang, Y. Zhou, Osteopontin in bone metabolism and bone diseases, Med. Sci. Monit. 26 (2020) e919159.

[41] N. Lv, Z. Zhou, M. Hou, L. Hong, H. Li, Z. Qian, X. Gao, M. Liu, Research progress of vascularization strategies of tissue-engineered bone, Front. Bioeng. Biotechnol. 11 (2023) 1291969.

[42] L. Wu, Y. Gu, L. Liu, J. Tang, J. Mao, K. Xi, Z. Jiang, Y. Zhou, Y. Xu, L. Deng, L. Chen, W. Cui, Hierarchical micro/nanofibrous membranes of sustained releasing VEGF for periosteal regeneration, Biomaterials 227 (2020) 119555.

[43] L. Batoon, A.J. Koh, S.M. Millard, J. Grewal, F.M. Choo, R. Kannan, A. Kinnaird, M. Avey, T. Teslya, A.R. Pettit, L.K. McCauley, H. Roca, Induction of osteoblast apoptosis stimulates macrophage efferocytosis and paradoxical bone formation, Bone Res 12 (1) (2024) 43.

[44] J. Li, W. Hou, Y. Yang, Q. Deng, H. Fu, Y. Yin, K. Duan, B. Feng, T. Guo, J. Weng, Micro/nano-topography promotes osteogenic differentiation of bone marrow stem cells by regulating periostin expression, Colloids Surf. B Biointerfaces 218 (2022) 112700.

[45] M.E. Pickering, C. Oris, R. Chapurlat, Periostin in osteoporosis and Cardiovascular disease, J Endocr Soc 7 (7) (2023) bvad081.

[46] T. Chen, Y. Peng, W. Hu, H. Shi, P. Li, Y. Que, J. Qiu, X. Qiu, B. Gao, H. Zhou, Y. Chen, Y. Zhu, S. Li, A. Liang, W. Gao, D. Huang, Irisin enhances chondrogenic differentiation of human mesenchymal stem cells via Rap1/PI3K/AKT axis, Stem Cell Res. Ther. 13 (1) (2022) 392.

[47] Y. Yang, J. Rao, H. Liu, Z. Dong, Z. Zhang, H.P. Bei, C. Wen, X. Zhao, Biomimicking design of artificial periosteum for promoting bone healing, J Orthop Translat 36 (2022) 18–32.

[48] W. Liu, K. Zhang, J. Nan, P. Lei, Y. Sun, Y. Hu, Nano artificial periosteum PCL/Ta/ZnO accelerates repair of periosteum via antibacterial, promoting vascularization and osteogenesis, Biomater. Adv. 154 (2023) 213624.

[49] E. Mariani, G. Lisignoli, R.M. Borzi, L. Pulsatelli, Biomaterials: foreign bodies or tuners for the immune response? Int. J. Mol. Sci. 20 (3) (2019).

[50] H. Xing, H. Lee, L. Luo, T.R. Kyriakides, Extracellular matrix-derived biomaterials in engineering cell function, Biotechnol. Adv. 42 (2020) 107421.

[51] C. Lu, T. Miclau, D. Hu, E. Hansen, K. Tsui, C. Puttlitz, R.S. Marcucio, Cellular basis for age-related changes in fracture repair, J. Orthop. Res. 23 (6) (2005) 1300–1307.

[52] J. Guo, F. Wang, Y. Hu, Y. Luo, Y. Wei, K. Xu, H. Zhang, H. Liu, L. Bo, S. Lv, S. Sheng, X. Zhuang, T. Zhang, C. Xu, X. Chen, J. Su, Exosome-based bone-targeting drug delivery alleviates impaired osteoblastic bone formation and bone loss in inflammatory bowel diseases, Cell Rep Med 4 (1) (2023) 100881.

[53] J. Munoz, N.S. Akhavan, A.P. Mullins, B.H. Arjmandi, Macrophage polarization and osteoporosis: a review, Nutrients 12 (10) (2020).

[54] J. Wang, C. Zhang, W. Zhang, W. Liu, Y. Guo, P. Dang, L. Wei, H. Zhao, X. Deng, S. Guo, L. Chen, Ultrathin WOx nanoribbons with moderate ROS clearance and antibacterial abilities efficiently induce M2 macrophage polarization for diabetic bone defect repair, Adv. Funct. Mater. 34 (8) (2024) 2306319.

[55] R. Klopfleisch, Macrophage reaction against biomaterials in the mouse model - phenotypes, functions and markers, Acta Biomater. 43 (2016) 3–13.

[56] Y. Wang, Q. Lin, H. Zhang, S. Wang, J. Cui, Y. Hu, J. Liu, M. Li, K. Zhang, F. Zhou, Y. Jing, Z. Geng, J. Su, M2 macrophage-derived exosomes promote diabetic fracture healing by acting as an immunomodulator, Bioact. Mater. 28 (2023) 273–283.

[57] Y. Lei, Y. Wang, J. Shen, Z. Cai, Y. Zeng, P. Zhao, J. Liao, C. Lian, N. Hu, X. Luo, W. Cui, W. Huang, Stem cell-recruiting injectable microgels for repairing osteoarthritis, Adv. Funct. Mater. 31 (48) (2021) 2105084.

[58] F. Shang, Y. Yu, S. Liu, L. Ming, Y. Zhang, Z. Zhou, J. Zhao, Y. Jin, Advancing application of mesenchymal stem cell-based bone tissue regeneration, Bioact. Mater. 6 (3) (2021) 666–683.

[59] D.S. Chulpanova, K.V. Kitaeva, L.G. Tazetdinova, V. James, A.A. Rizvanov, V. V. Solovyeva, Application of mesenchymal stem cells for therapeutic agent delivery in anti-tumor treatment, Front. Pharmacol. 9 (2018) 259.

[60] X. Ma, J. Chen, J. Liu, B. Xu, X. Liang, X. Yang, Y. Feng, X. Liang, J. Liu, IL-8/CXCR2 mediates tropism of human bone marrow-derived mesenchymal stem cells toward CD133(+)/CD44(+) Colon cancer stem cells, J. Cell. Physiol. 236 (4) (2021) 3114–3128.

[61] M.O. Schar, J. Diaz-Romero, S. Kohl, M.A. Zumstein, D. Nesic, Platelet-rich concentrates differentially release growth factors and induce cell migration in vitro, Clin. Orthop. Relat. Res. 473 (5) (2015) 1635–1643.

[62] H. Zhang, X. Li, J. Li, L. Zhong, X. Chen, S. Chen, SDF-1 mediates mesenchymal stem cell recruitment and migration via the SDF-1/CXCR4 axis in bone defect, J. Bone Miner. Metabol. 39 (2) (2021) 126–138.

[63] S. Liu, Y. Liu, L. Jiang, Z. Li, S. Lee, C. Liu, J. Wang, J. Zhang, Recombinant human BMP-2 accelerates the migration of bone marrow mesenchymal stem cells via the CDC42/PAK1/LIMK1 pathway in vitro and in vivo, Biomater. Sci. 7 (1) (2018) 362–372.

[64] Y. Miao, X. Liu, J. Luo, Q. Yang, Y. Chen, Y. Wang, Double-network DNA macroporous hydrogel enables aptamer-directed cell recruitment to accelerate bone healing, Adv. Sci. 11 (1) (2024) e2303637.

[65] J.S. Gong, G.Q. Zhu, Y. Zhang, B. Chen, Y.W. Liu, H.M. Li, Z.H. He, J.T. Zou, Y. X. Qian, S. Zhu, X.Y. Hu, S.S. Rao, J. Cao, H. Xie, Z.X. Wang, W. Du, Aptamer-functionalized hydrogels promote bone healing by selectively recruiting endogenous bone marrow mesenchymal stem cells, Mater Today Bio 23 (2023) 100854.

[66] T. Sun, C. Meng, Q. Ding, K. Yu, X. Zhang, W. Zhang, W. Tian, Q. Zhang, X. Guo, B. Wu, Z. Xiong, In situ bone regeneration with sequential delivery of aptamer and BMP2 from an ECM-based scaffold fabricated by cryogenic free-form extrusion, Bioact. Mater. 6 (11) (2021) 4163–4175.

[67] M. Richter, P. Vader, G. Fuhrmann, Approaches to surface engineering of extracellular vesicles, Adv. Drug Deliv. Rev. 173 (2021) 416–426.

[68] L. Bai, P. Song, J. Su, Bioactive elements manipulate bone regeneration, Biomater Transl 4 (4) (2023) 248–269.

[69] Y. Liu, J.K. Chan, S.H. Teoh, Review of vascularised bone tissue-engineering strategies with a focus on co-culture systems, J. Tissue. Eng. Regen. Med 9 (2) (2015) 85–105.

[70] E. Ellermann, N. Meyer, R.E. Cameron, S.M. Best, In vitro angiogenesis in response to biomaterial properties for bone tissue engineering: a review of the state of the art, Regen. Biomater 10 (2023) rbad027.

[71] J. Pajarinen, T. Lin, E. Gibon, Y. Kohno, M. Maruyama, K. Nathan, L. Lu, Z. Yao, S. B. Goodman, Mesenchymal stem cell-macrophage crosstalk and bone healing, Biomaterials 196 (2019) 80–89.

[72] K. Archacka, I. Grabowska, B. Mierzejewski, J. Graffstein, A. Gorzynska, M. Krawczyk, A.M. Rozycka, I. Kalaszczynska, G. Muras, W. Streminska, K. Janczyk-Ilach, P. Walczak, M. Janowski, M.A. Ciemerych, E. Brzoska, Hypoxia preconditioned bone marrow-derived mesenchymal stromal/stem cells enhance myoblast fusion and skeletal muscle regeneration, Stem Cell Res. Ther. 12 (1) (2021) 448.

[73] O. Duchamp de Lageneste, A. Julien, R. Abou-Khalil, G. Frangi, C. Carvalho, N. Cagnard, C. Cordier, S.J. Conway, C. Colnot, Periosteum contains skeletal stem cells with high bone regenerative potential controlled by Periostin, Nat. Commun. 9 (1) (2018) 773.

[74] S.C. Heo, W.C. Shin, M.J. Lee, B.R. Kim, I.H. Jang, E.J. Choi, J.S. Lee, J.H. Kim, Periostin accelerates bone healing mediated by human mesenchymal stem cell-embedded hydroxyapatite/tricalcium phosphate scaffold, PLoS One 10 (3) (2015) e0116698.

[75] S.J. Zhao, F.Q. Kong, J. Jie, Q. Li, H. Liu, A.D. Xu, Y.Q. Yang, B. Jiang, D.D. Wang, Z.Q. Zhou, P.Y. Tang, J. Chen, Q. Wang, Z. Zhou, Q. Chen, G.Y. Yin, H.W. Zhang, J. Fan, Macrophage MSR1 promotes BMSC osteogenic differentiation and M2-like

polarization by activating PI3K/AKT/GSK3beta/beta-catenin pathway, Theranostics 10 (1) (2020) 17–35.

[76] B. Boettner, L. Van Aelst, Control of cell adhesion dynamics by Rap1 signaling, Curr. Opin. Cell Biol. 21 (5) (2009) 684–693.

[77] M.R. Gold, R.J. Ingham, S.J. McLeod, S.L. Christian, M.P. Scheid, V. Duronio, L. Santos, L. Matsuuchi, Targets of B-cell antigen receptor signaling: the phosphatidylinositol 3-kinase/Akt/glycogen synthase kinase-3 signaling pathway and the Rap1 GTPase, Immunol. Rev. 176 (2000) 47–68.

[78] S. Shah, E.J. Brock, K. Ji, R.R. Mattingly, Ras and Rap1: a tale of two GTPases, Semin. Cancer Biol. 54 (2019) 29–39.

[79] K. Sun, J. Luo, J. Guo, X. Yao, X. Jing, F. Guo, The PI3K/AKT/mTOR signaling pathway in osteoarthritis: a narrative review, Osteoarthr. Cartil. 28 (4) (2020) 400–409.

[80] L. Li, W. Jiang, B. Yu, H. Liang, S. Mao, X. Hu, Y. Feng, J. Xu, L. Chu, Quercetin improves cerebral ischemia/reperfusion injury by promoting microglia/macrophages M2 polarization via regulating PI3K/Akt/NF-kappaB signaling pathway, Biomed. Pharmacother. 168 (2023) 115653.

[81] Y. Xu, S. Chen, L. Huang, W. Han, Y. Shao, M. Chen, Y. Zhang, R. He, B. Xie, Epimedin C alleviates glucocorticoid-induced suppression of osteogenic differentiation by modulating PI3K/AKT/RUNX2 signaling pathway, Front. Pharmacol. 13 (2022) 894832.

[82] T. Fujita, Y. Azuma, R. Fukuyama, Y. Hattori, C. Yoshida, M. Koida, K. Ogita, T. Komori, Runx2 induces osteoblast and chondrocyte differentiation and enhances their migration by coupling with PI3K-Akt signaling, J. Cell Biol. 166 (1) (2004) 85–95.

[83] H.J. Wang, H.F. Ran, Y. Yin, X.G. Xu, B.X. Jiang, S.Q. Yu, Y.J. Chen, H.J. Ren, S. Feng, J.F. Zhang, Y. Chen, Q. Xue, X.Y. Xu, Catalpol improves impaired neurovascular unit in ischemic stroke rats via enhancing VEGF-PI3K/AKT and VEGF-MEK1/2/ERK1/2 signaling, Acta Pharmacol. Sin. 43 (7) (2022) 1670–1685.

[84] Y. Lin, Y. Jiang, H. Xian, X. Cai, T. Wang, Expression and correlation of the Pi3k/Akt pathway and VEGF in oral submucous fibrosis, Cell Prolif. 56 (11) (2023) e13491.

[85] S. Rayamajhi, S. Aryal, Surface functionalization strategies of extracellular vesicles, J. Mater. Chem. B 8 (21) (2020) 4552–4569.